

Effects of the semi-local Reynolds number in scaling turbulent statistics for wall heated/cooled supersonic turbulent boundary layers

Hirai, Ryo; Pecnik, Rene; Kawai, Soshi

DOI

[10.1103/PhysRevFluids.6.124603](https://doi.org/10.1103/PhysRevFluids.6.124603)

Publication date

2021

Document Version

Final published version

Published in

Physical Review Fluids

Citation (APA)

Hirai, R., Pecnik, R., & Kawai, S. (2021). Effects of the semi-local Reynolds number in scaling turbulent statistics for wall heated/cooled supersonic turbulent boundary layers. *Physical Review Fluids*, 6(12), Article 124603. <https://doi.org/10.1103/PhysRevFluids.6.124603>

Important note

To cite this publication, please use the final published version (if applicable). Please check the document version above.

Copyright

Other than for strictly personal use, it is not permitted to download, forward or distribute the text or part of it, without the consent of the author(s) and/or copyright holder(s), unless the work is under an open content license such as Creative Commons.

Takedown policy

Please contact us and provide details if you believe this document breaches copyrights. We will remove access to the work immediately and investigate your claim.

Effects of the semi-local Reynolds number in scaling turbulent statistics for wall heated/cooled supersonic turbulent boundary layers

Ryo Hirai ^{1,*}, Rene Pecnik,² and Soshi Kawai¹¹*Department of Aerospace Engineering, Tohoku University, Sendai, Miyagi, 980-8579, Japan*²*Process and Energy Department, Delft University of Technology, Leeghwaterstraat 39, 2628 CB Delft, the Netherlands*

(Received 25 March 2021; accepted 9 November 2021; published 13 December 2021)

In supersonic turbulent boundary layers over isothermal walls, we investigate how the wall heat flux affects turbulent statistics and velocity scaling laws. To distinguish local Reynolds number and compressibility effects, we consider a conventional ideal gas with Sutherland's law and a fluid for which the dynamic viscosity is proportional to the square root of density, such that the semi-local Reynolds number is constant in the wall-normal direction. The results clearly indicate that the changes of the semi-local Reynolds number within the boundary layer affect the coherent turbulent structures, which induces the deviation of the viscous stress, Reynolds stress, and semi-local transformed mean velocity between different wall temperature conditions. For the cases with constant semi-local Reynolds number, we observe that the wall heat flux does not affect the turbulent structures and that the velocity profiles perfectly collapse among each other, indicating the importance of the semi-local Reynolds number, rather than the temperature or density themselves, on turbulent statistics and structures. Also, the conditional averaged analysis for the near-wall turbulent phenomena indicates a clear relationship between the turbulent structures and the mean velocity gradients. Additionally, an existing analytical temperature-velocity relation is verified based on the examinations of the applied equilibrium flow assumptions, and the results explain the disagreement between the present data and the analytical solutions in the outer boundary layer region, especially for isothermal wall cases.

DOI: [10.1103/PhysRevFluids.6.124603](https://doi.org/10.1103/PhysRevFluids.6.124603)

I. INTRODUCTION

Wall-bounded turbulent flows with wall heat transfer appear in many engineering applications. Common examples are nozzles in rocket engines, combustion chambers in gas turbines, or heat exchangers in virtually any energy conversion system. In these applications, the wall temperature or the wall heat transfer rate often becomes one of the design constraints, and near-wall turbulence plays a significant role in increasing the thermal conductivity characteristics of fluids by its turbulent thermal diffusion effects. Too high temperature can cause material damage and consequently failure of the device, and yields structural failures or decrease in performances of the fluid machinery. Therefore, wall turbulence must be predicted accurately to assure the safety of thermal-fluid systems, which require a detailed understanding of turbulent physics in wall-heated or -cooled flows.

Thermal properties of wall-bounded turbulent flows have been investigated theoretically, experimentally, and numerically in the past decades. In incompressible flows, which have negligible variations in thermophysical properties, the temperature is a passive scalar and does not influence

*Corresponding author: ryo.hirai.q7@dc.tohoku.ac.jp

turbulent dynamics. On the other hand, the higher the flow speed, the larger the variations in thermophysical properties, which result in nonlinear couplings between kinetic and thermal quantities that make the estimations of the velocity and temperature fields difficult [1,2]. Therefore, physical relationships between velocity and temperature based on the momentum or energy transport have been addressed and proposed, and the typical example is the Reynolds analogy [3–5] for mean physical quantities. The original Reynolds analogy [3] was obtained for incompressible flows, which has been modified for compressible flows as the Crocco-Busemann relation [4] or turbulent boundary layers as Walz’s equation [5]. Walz’s equation often has been applied to wall-heated or -cooled flows, and many studies have reported the good performance of the equation [6–8]. On the other hand, regarding the turbulent fluctuations, relationships between the streamwise velocity fluctuations and the temperature fluctuations have been proposed and called the strong Reynolds analogy (SRA) [6,9–15]. The original SRA [9] also has been extended for several flow conditions and some modified SRAs that can consider wall heat flux effects have been proposed by Huang *et al.* [13] (Huang’s modified SRA, HSRA) or Guarini *et al.* [14]. HSRA has given the collapsed profiles under various wall temperature conditions, shown in Refs. [16–18]. Further, Zhang *et al.* [15] proposed the generalized Reynolds analogy based on a formal generalization of the SRA, and it has shown improvements compared with Walz’s equation, in the cooled-wall hypersonic case [17,19].

The other universal theory in wall turbulence is scaling laws that make physical quantity profiles, such as velocity [20–24], temperature [20], or Reynolds stress collapse for several flow conditions. Especially for the mean velocity, the representative scaling theory is the law of the wall for the incompressible condition, proposed by Kármán, which uses the velocity and wall-normal coordinate nondimensionalized by wall quantities as

$$\bar{u}^+ = \frac{\bar{u}}{\bar{u}_\tau}, \quad y^+ = \frac{y}{l_v}, \quad (1)$$

where \bar{u} is the mean velocity, y is the wall-normal coordinate, $\bar{u}_\tau = \sqrt{\bar{\tau}_w/\bar{\rho}_w}$ is the friction velocity, $l_v = \bar{\mu}_w/(\bar{\rho}_w\bar{u}_\tau)$ is the viscous length scale, $\bar{\rho}$ is the density, $\bar{\mu}$ is the dynamic viscosity, $\bar{\tau}$ is the viscous stress, and the subscript w denotes the quantities at the wall. Later, the van Driest transformation [24], which can be applied to compressible flows by taking account of density variations, has been proposed as

$$\bar{u}_{vD}^+ = \int_0^{\bar{u}^+} \sqrt{\frac{\bar{\rho}}{\bar{\rho}_w}} d\bar{u}^+. \quad (2)$$

The accuracy of the van Driest transformation has been reported for a large range of Reynolds or Mach numbers, for adiabatic-wall flows [6]. However, in wall-heated or -cooled turbulent flow cases, disagreements of the van Driest transformed velocity profiles have been reported [25–27] so that the more proper transformation is required. Regarding the length scale y^+ in Eq. (1), many previous studies have shown that a better collapse for different wall temperature cases can be obtained by replacing it with the semi-local length scale [28] given as [17,25,27,29]

$$y^* = \frac{\sqrt{\bar{\rho}}\sqrt{\bar{\tau}_w}y}{\bar{\mu}}. \quad (3)$$

Also for the velocity scale \bar{u}_{vD}^+ , Trettel and Larsson [22] and Patel *et al.* [23] recently proposed an extension of the van Driest transformation that utilizes the effectiveness of the semi-local length scaling as

$$\bar{u}^* = \int_0^{\bar{u}_{vD}^+} \left(1 + \frac{y}{\text{Re}_\tau^*} \frac{d\text{Re}_\tau^*}{dy}\right) d\bar{u}_{vD}^+ = \int_0^{\bar{u}^+} \left(\frac{\bar{\rho}}{\bar{\rho}_w}\right)^{1/2} \left(1 + \frac{1}{2} \frac{y}{\bar{\rho}} \frac{d\bar{\rho}}{dy} - \frac{y}{\bar{\mu}} \frac{d\bar{\mu}}{dy}\right) d\bar{u}^+, \quad (4)$$

where $\text{Re}_\tau^* = \sqrt{\bar{\rho}}\sqrt{\bar{\tau}_w}\delta_{99}/\bar{\mu}$ is the semi-local Reynolds number. This transformation successfully obtains the better collapse of mean velocity profiles for almost the entire inner layer. However, Eq. (4) still shows some disagreements from the ideal universal profiles, as reported in Refs. [27,30,31]. Huang *et al.* [30] performed cooled-wall hypersonic $\text{Ma}_\infty = 11, 14$ turbulent boundary layer simulations and reported an upwards shift of the transformed velocity profiles in the inertial sublayer, compared with that of quasi-adiabatic-wall supersonic boundary layers. Volpiani *et al.* [31] also reported the upwards shift in the inertial sublayer of heated-wall hypersonic $\text{Ma}_\infty = 5$ turbulent boundary layers. The cause of these disagreements appears to depend on several factors: the degree of wall heating or cooling, Mach number, or inherent differences in channels or boundary layers. However, a clear insight on the cause is still missing.

In the present work, we further investigate wall-heated or -cooled supersonic turbulent boundary layers to identify key parameters affecting turbulence structures and the velocity scaling law. We performed large-eddy-simulations (LES) for three different wall-temperature conditions: quasi-adiabatic, heated, and cooled walls. To distinguish between effects related to Mach number and semi-local Reynolds number variations, we also performed simulations for which the semi-local Reynolds number is constant in the wall-normal direction. The present paper is arranged as follows. Numerical methods and settings are given in Sec. II. Case parameters of the present numerical simulations are given in Sec. III. Results are shown in Sec. IV; spatially developed temperature fields are verified through the analyses of the temperature-velocity relations (i.e., Walz's equation) in Sec. IV A; performances of mean-velocity transformations are reported in Sec. IV B; relationships between the extended van Driest transformation shown in Eq. (4) and viscous stress are derived in Sec. IV C; streamwise stress components that relate to viscous stress analytically are shown in Sec. IV D; finally, connections between turbulent statistics and turbulent structures are discussed in Sec. IV E. Conclusions are presented in Sec. V.

II. NUMERICAL METHODOLOGY

A. Governing equations and fluid properties

The simulations in the present paper are obtained by solving the spatially filtered compressible Navier-Stokes equations, which are given in differential form as

$$\frac{\partial \rho}{\partial t} + \frac{\partial(\rho u_j)}{\partial x_j} = 0, \quad (5)$$

$$\frac{\partial(\rho u_i)}{\partial t} + \frac{\partial(\rho u_i u_j + p \delta_{ij} - \tau_{ij})}{\partial x_j} = 0, \quad (6)$$

$$\frac{\partial(\rho E)}{\partial t} + \frac{\partial(\rho E u_j + p u_j + q_j - u_i \tau_{ij})}{\partial x_j} = 0, \quad (7)$$

where the quantities are spatially filtered, $x_i = (x, y, z)$ are the coordinates in the streamwise, wall-normal, and spanwise directions, $u_i = (u, v, w)$ are the corresponding velocity components, ρ is the fluid density, $E = e + u_i u_i / 2$ is the total energy, $e = p / (\rho(\gamma - 1))$ is the internal energy, $\gamma (=1.4)$ is the heat capacity ratio, $p = \rho R T$ is the pressure, R is the gas constant, T is the temperature, τ_{ij} is the viscous stress tensor, and q_j is the heat flux vector. The viscous stress tensor is

$$\tau_{ij} = 2(\mu + \mu_{\text{SGS}}) \left[\frac{1}{2} \left(\frac{\partial u_i}{\partial x_j} + \frac{\partial u_j}{\partial x_i} \right) - \frac{1}{3} \frac{\partial u_k}{\partial x_k} \delta_{ij} \right] \quad (8)$$

and the heat flux vector is

$$q_j = -\frac{1}{\gamma - 1} \left(\frac{\mu}{\text{Pr}} + \frac{\mu_{\text{SGS}}}{\text{Pr}_{\text{SGS}}} \right) \frac{\partial a^2}{\partial x_j}, \quad (9)$$

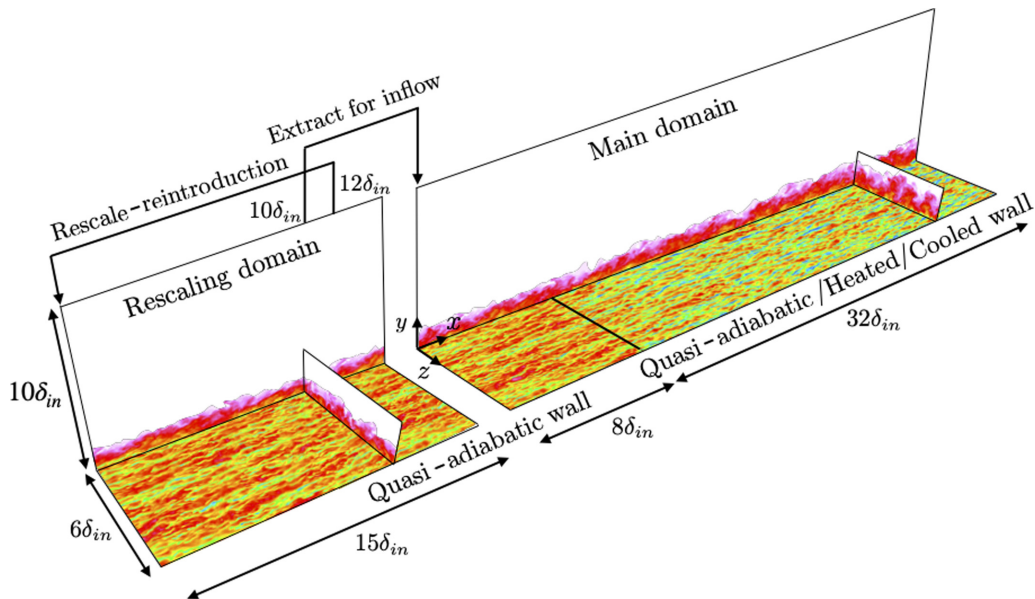


FIG. 1. Computational domains of the present large eddy simulations of the zero-pressure gradient turbulent boundary layer with heated and cooled walls. δ_{in} is the time-averaged boundary layer thickness at the inlet of the rescaling domain. Streamwise velocity contours at side, cross, and wall-parallel planes.

where a is the speed of sound, μ is the dynamic viscosity, $Pr(=0.72)$ is the Prandtl number, μ_{SGS} is the subgrid-scale dynamic viscosity, and $Pr_{SGS}(=0.9)$ is the subgrid-scale turbulent Prandtl number.

In this paper, two approaches are used to specify the dynamic viscosity μ . The first one is based on Sutherland's law, which uses the kinetic theory of ideal gases and the idealized intermolecular potential. Sutherland's law is commonly used for ideal gases as

$$\frac{\mu}{\mu_{\infty}} = \left(\frac{T}{T_{\infty}}\right)^{\frac{3}{2}} \frac{T_{\infty} + T_1}{T + T_1}, \quad (10)$$

where the subscript ∞ denotes the freestream quantities, $T_1 = 110.4$ K, and $T_{\infty} = 255.0$ K.

The second approach of setting the dynamic viscosity ensures that the semi-local Reynolds number, defined as

$$Re_{\tau}^* = \sqrt{\frac{\rho}{\rho_w} \frac{\mu_w}{\mu}} Re_{\tau}, \quad (11)$$

where the subscript w denotes the quantities at the wall, remains constant within the boundary layer. In Eq. (11), $Re_{\tau} = \sqrt{\rho_w} \sqrt{\tau_w} \delta_{99} / \mu_w$ is the friction Reynolds number, with the 99% freestream velocity boundary layer thickness δ_{99} . The semi-local Reynolds number Re_{τ}^* can be considered as a similarity parameter of flows with thermophysical property variations, which has been discussed in the previous research [23,32]. For ensuring a constant value of Re_{τ}^* , the dynamic viscosity is thus set proportional to the square root of the fluid density as

$$\frac{\mu}{\mu_{\infty}} = \sqrt{\frac{\rho}{\rho_{\infty}}}. \quad (12)$$

B. Case setup and numerical methods

Figure 1 shows the schematic of the present simulations, which represent the setup of zero-pressure-gradient turbulent boundary layers. The computational domain is divided into the rescaling

TABLE I. Reynolds number, Mach number, wall temperature, and abbreviation for all cases. Black, quasiadiabatic; red, heated; blue, cooled; gray, incompressible as references. Solid, ideal gas cases used Sutherland's law Eq. (10); dashed, constant Re_τ^* cases used Eq. (12).

| Case | Re_τ | Ma_∞ | T_w/T_r | T_w/T_∞ | Abbrev. | Line style |
|--------------------------------------|-----------|-------------|-----------|----------------|---------|-------------|
| Quasiadiabatic | 650 | 2.28 | 1.0 | 1.93 | AD | — |
| Heated | 305 | 2.28 | 2.0 | 3.84 | HE | — |
| Cooled | 1515 | 2.28 | 0.5 | 0.97 | CO | — |
| Quasiadiabatic, constant Re_τ^* | 566 | 2.28 | 1.0 | 1.93 | ADcRe | - - - - - |
| Heated, constant Re_τ^* | 505 | 2.28 | 2.0 | 3.84 | HEcRe | - . - . - . |
| Cooled, constant Re_τ^* | 654 | 2.28 | 0.5 | 0.97 | COcRe | - . - . - . |
| Incompressible high Re [41] | 1437 | | 1.0 | 1.0 | IncHi | - |
| Incompressible low Re [42] | 578 | | 1.0 | 1.0 | IncLo | - |

domain (left domain in Fig. 1) and the main domain (right domain in Fig. 1). The size of the rescaling domain is $(L_x, L_y, L_z) = (15\delta_{in}, 10\delta_{in}, 6\delta_{in})$, and that of the main domain is $(L_x, L_y, L_z) = (40\delta_{in}, 10\delta_{in}, 6\delta_{in})$ in streamwise (x), wall-normal (y), and spanwise (z) directions, respectively. Note that δ_{in} denotes the time-averaged boundary layer thickness at the inlet location of the rescaling domain.

The incoming boundary conditions of the rescaling domain are taken from a position $12\delta_{in}$ downstream of the inlet by using the rescaling-reintroduction method of Urbin and Knight [33]. Also, the incoming flow of the main domain is taken from $10\delta_{in}$ of the rescaling domain. Isothermal wall temperature conditions are given to the lower walls for both domains. The wall temperatures T_w are chosen based on the recovery temperature as

$$T_r = T_\infty \left[1 + (\gamma - 1)r \frac{M_\infty^2}{2} \right], \quad (13)$$

where $r(=0.9)$ is the recovery coefficient. At the rescaling domain, wall temperatures are fixed as a quasiadiabatic condition $T_w = T_r$. At the main domain, specifying the recovery temperature ratio $s = T_w/T_r$, the wall temperature transitions smoothly from the quasiadiabatic to the heated ($s > 1.0$) or cooled ($s < 1.0$) condition by using a hyperbolic tangent function as

$$T_w(x) = T_r \left[1 + \frac{s-1}{2} \left(1 + \tanh \frac{2(x-x_{trans})}{\delta_{in}} \right) \right], \quad (14)$$

where $x_{trans} = 8\delta_{in}$ is the transition position of wall temperature [34]. The wall to recovery temperature ratios for all cases are summarized in Table I. The wall boundary condition is the isothermal nonslip condition and the periodic boundary condition is imposed in the spanwise direction. The grid spacing is uniform in both streamwise and spanwise directions, while a stretched grid is used in the wall-normal direction with a maximum grid stretching ratio of 1.044 within the boundary layers and 1.079 at the freestream regions, respectively. More details of the mesh resolutions for the different cases are shown in Table II. All the results presented in this study are at the station of $33\delta_{in}$ downstream of the main domain, unless otherwise noted. .

A sixth-order compact finite difference scheme is used [35] to compute the spatial derivatives, coupled with an eighth-order compact low-pass filter [35,36], with the filter parameter α_f fixed at 0.49, to prevent numerical instabilities. Our prior studies [37,38] suggest the appropriateness of the employed α_f for turbulent flow computations. The equations are integrated in time using a third-order TVD Runge-Kutta method [39], and a selective-mixed-scale model [40] is used to compute the subgrid-scale dynamic viscosity μ_{SGS} . We note that, although the subgrid-scale model is used in this study, the contributions of the subgrid-scale stresses are negligible throughout the

TABLE II. Number of grid points N_x , N_y , and N_z , and spatial mesh resolutions Δx , Δy , and Δz . η , Kolmogorov length scale. Δy^+ is extracted at uniform grid spacing outer-boundary layer regions.

| Abbrev. | N_x | N_y | N_z | Δx^+ | Δy_w^+ | Δy^+ | Δz^+ | $(\Delta x/\eta)_{\max}$ | $(\Delta y/\eta)_{\max}$ | $(\Delta z/\eta)_{\max}$ |
|---------|-------|-------|-------|--------------|----------------|--------------|--------------|--------------------------|--------------------------|--------------------------|
| AD | 1601 | 182 | 491 | 10.05 | 0.80 | 8.94 | 5.02 | 7.10 | 0.57 | 3.55 |
| HE | 1601 | 182 | 491 | 4.24 | 0.34 | 3.78 | 2.12 | 3.08 | 0.25 | 1.54 |
| CO | 2801 | 254 | 851 | 14.09 | 0.79 | 16.45 | 7.04 | 9.87 | 0.55 | 4.93 |
| ADcRe | 1601 | 182 | 491 | 9.30 | 0.74 | 8.27 | 4.65 | 6.47 | 0.52 | 3.24 |
| HEcRe | 1601 | 182 | 491 | 7.83 | 0.63 | 6.97 | 3.92 | 5.43 | 0.43 | 2.71 |
| COcRe | 2801 | 254 | 851 | 6.18 | 0.35 | 7.21 | 3.09 | 4.28 | 0.24 | 2.14 |

boundary layers, due to the sufficiently fine grid resolutions employed in this study, as will be discussed in Table II.

III. CASE DESCRIPTION

Several heated and cooled developed boundary layers have been considered in this study to investigate the influence of thermophysical property variations on turbulent statistics and their self-similar scaling characteristics. The cases are summarized in Table I, where all six compressible boundary layer simulations are performed under the assumption of a calorically perfect gas using the ideal equation of state and assuming constant specific heats. Three different thermal wall conditions have been considered, namely, a quasiadiabatic (black line), a heated (red), and a cooled (blue) isothermal wall temperature. For the first three cases, indicated by solid lines in the subsequent discussions, the dynamic viscosity follows Sutherland's law as given in Eq. (10). These cases are referred to hereafter as ideal gas cases. For the second set of three simulations, indicated by dashed lines, the dynamic viscosity is proportional to the square root of density as defined by Eq. (12). For these cases, the semi-local Reynolds number Re_τ^* is constant in the wall-normal direction and they are referred to as constant Re_τ^* (cRe) cases. The last two cases correspond to incompressible boundary layers at different Reynolds numbers from Refs. [41,42] and are used as references for comparison.

Figure 2 shows the distributions of mean density and dynamic viscosity, both normalized by their respective freestream values. The heated cases show the largest variations of both density and dynamic viscosity due to the large increase of temperature within the boundary layers. In the adiabatic cases, the density and viscosity change within the boundary layers because of the viscous

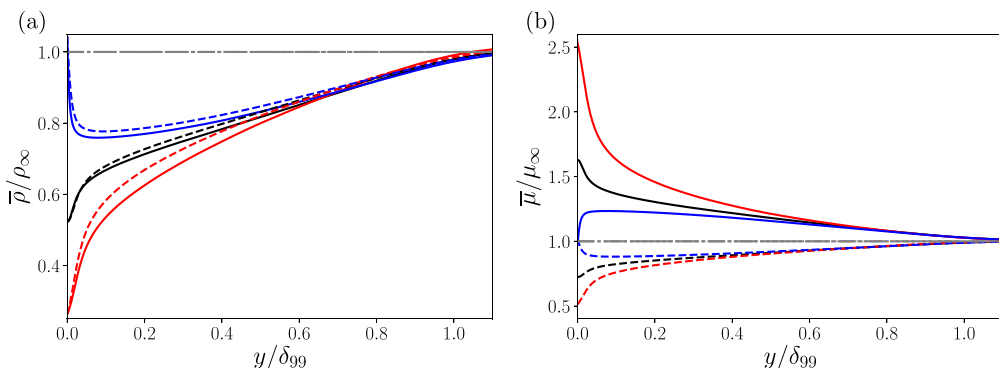


FIG. 2. Distributions of (a) mean density $\bar{\rho}/\rho_\infty$ and (b) mean dynamic viscosity $\bar{\mu}/\mu_\infty$. Lines as in Table I. Both two lines of incompressible cases overlap each other.

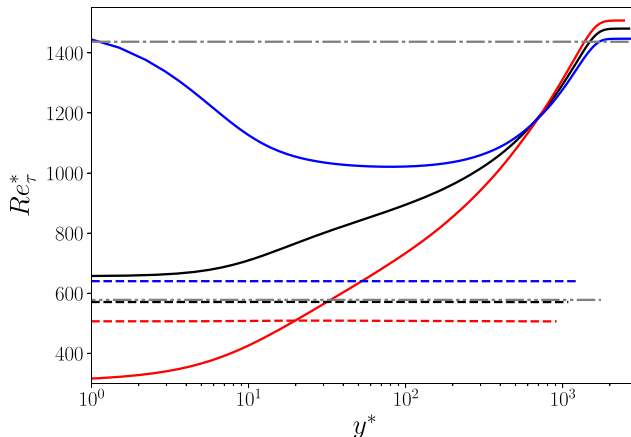


FIG. 3. Distributions of semi-local Reynolds number Re_τ^* . Lines as in Table I.

heating, although the changes are smaller compared to the heated cases. On the other hand, the cooled cases show a local peak value in both density and dynamic viscosity, because the wall value is approximately the same as the freestream value. Regarding the constant Re_τ^* cases (dashed lines), their density distributions are similar to the ideal gas cases (solid lines) in Fig. 2(a). However, as for the dynamic viscosity distributions shown in Fig. 2(b), the constant Re_τ^* cases show the opposite behavior to the ideal gas cases due to the different dynamic viscosity formulation given in Eq. (12).

Figure 3 shows the distributions of the semi-local Reynolds number, Re_τ^* . The ideal gas cases, indicated by solid lines, show similar characteristics as the density shown in Fig. 2(a). By design, the constant Re_τ^* cases, indicated by dashed lines, have a constant distribution of Re_τ^* . The two incompressible cases are chosen such that their Reynolds numbers are either comparable to the constant Re_τ^* cases or to the freestream value of Re_τ^* of the ideal gas cases.

Table II shows the number of grid points and spatial mesh resolutions for all cases. The spatial resolutions are evaluated in wall units Δx^+ , Δy^+ , and Δz^+ , or by comparisons with the Kolmogorov length scale $\eta = [(\bar{\mu}/\bar{\rho})^3/(\bar{\epsilon}/\bar{\rho})]^{0.25}$, where $\bar{\epsilon}$ is the local dissipation rate of turbulent kinetic energy. The spatial resolutions are comparable to those used in previous works of DNS [23,43], which satisfy the $\Delta x < 12\eta$, $\Delta y < 2\eta$, and $\Delta z < 6\eta$, and thus the present numerical grids are sufficiently fine for LES.

IV. RESULTS AND DISCUSSIONS

First, the spatially developed temperature field of the compressible cases in Table I is verified through the analyses of the temperature-velocity relations. Second, the cases are analyzed based on their scaled mean velocity profiles and differences are highlighted. Third, the total shear stress balance is compared among the cases and the consequence of keeping Re_τ^* constant is investigated. Fourth, we discuss changes in turbulence structures for all ideal gas and constant Re_τ^* cases, which provides a clarification for the observation made in the stress balance. Finally, we will suggest a coupling relation between the turbulent structure changes and the velocity gradient features. In the following, the turbulent statistics are computed by averaging in time for a time interval of more than $246\delta_{in}/u_\infty$ as well as in the homogeneous spanwise direction to ensure convergence of flow statistics, where \bar{f} and f denote the Reynolds and Favre averaging quantities where $f = \bar{f} + f'$ and $f = \bar{f} + f''$.

A. Spatially developed temperature field: Temperature-velocity relations

The spatially developed temperature field in compressible flow cases is verified through the analyses of the temperature-velocity profiles compared with Walz's equation. Walz's equation [5] describes the temperature-velocity relationship as

$$\frac{\bar{T}}{T_\infty} = \frac{\bar{T}_w}{T_\infty} + \frac{T_r - \bar{T}_w}{T_\infty} \frac{\bar{u}}{u_\infty} + \frac{T_\infty - T_r}{T_\infty} \left(\frac{\bar{u}}{u_\infty} \right)^2, \quad (15)$$

where T_r is the recovery temperature shown in Eq. (13). This relation is obtained from the total energy equation in Eq. (7). By assuming the inner layer of developed equilibrium boundary layers (i.e., parallel flow and no pressure gradient assumptions), the averaged energy equation becomes

$$\frac{d}{dy} \left[(\bar{\mu} + \bar{\mu}_t) \bar{u} \frac{d\bar{u}}{dy} + C_p \left(\frac{\bar{\mu}}{\text{Pr}} + \frac{\bar{\mu}_t}{\text{Pr}_t} \right) \frac{d\bar{T}}{dy} \right] = 0, \quad (16)$$

where $\bar{\mu}_t$ is the RANS (Reynolds-averaged Navier-Stokes) turbulent viscosity and Pr_t is the RANS turbulent Prandtl number. After integrating in the wall-normal direction, one may obtain

$$\mu^* \bar{u} \frac{d\bar{u}}{dy} + C_p \frac{\mu^*}{\text{Pr}^*} \frac{d\bar{T}}{dy} = -\bar{q}_w, \quad (17)$$

where $\mu^* = \bar{\mu} + \bar{\mu}_t$, $\text{Pr}^* = \mu^*/(\bar{\mu}/\text{Pr} + \bar{\mu}_t/\text{Pr}_t)$, and $\bar{q}_w = -C_p(\mu_w^*/\text{Pr}_w^*)(d\bar{T}_w/dy)|_w$. Further, using $d\bar{u}^2/dy = 2\bar{u} d\bar{u}/dy$ and assuming Pr^* and C_p constant, it can be shown that

$$\frac{d(\frac{1}{2}\text{Pr}^*\bar{u}^2)}{dy} + \frac{d(C_p\bar{T})}{dy} = -\frac{\text{Pr}^*}{\mu^*} \bar{q}_w. \quad (18)$$

The additional assumption to obtain Walz's equation is the total stress balance obtained by the streamwise momentum equation in Eq. (6) under the equilibrium boundary layer assumption as

$$\bar{\tau}_w \approx \bar{\mu} \frac{d\bar{u}}{dy} - \bar{\rho} u'' v'' \approx (\bar{\mu} + \bar{\mu}_t) \frac{d\bar{u}}{dy} = \mu^* \frac{d\bar{u}}{dy}, \quad (19)$$

and thus Eq. (18) can be rewritten as

$$\frac{d(\frac{1}{2}\text{Pr}^*\bar{u}^2)}{dy} + \frac{d(C_p\bar{T})}{dy} = -\frac{\text{Pr}^*\bar{q}_w}{\bar{\tau}_w} \frac{d\bar{u}}{dy}. \quad (20)$$

Equation (20) is again integrated in a wall-normal direction by assuming the $\text{Pr}^*\bar{q}_w/\bar{\tau}_w$ constant

$$\frac{1}{2}\text{Pr}^*\bar{u}^2 + C_p(\bar{T} - \bar{T}_w) = -\frac{\text{Pr}^*\bar{q}_w}{\bar{\tau}_w} \bar{u}. \quad (21)$$

By assuming adiabatic wall conditions (i.e., $\bar{q}_w = 0$) and defining the \bar{T} and \bar{u} as the freestream values (T_∞ and u_∞), here the relation between the wall temperature and freestream velocity can be obtained as

$$\bar{T}_w = T_\infty + \frac{1}{2} \frac{\text{Pr}^*}{C_p} u_\infty^2 = T_r \quad [\text{if } \text{Pr}^* = r = (0.9)]. \quad (22)$$

The \bar{T}_w in Eq. (22) is equivalent with the recovery temperature T_r shown in Eq. (13) when the mixed Prandtl number Pr^* is given as a constant recovery coefficient ($=0.9$). Subtracting Eq. (22) from Eq. (21) and transforming Eq. (22), the following equations can be obtained:

$$\frac{\text{Pr}^*\bar{q}_w}{C_p\bar{\tau}_w} = \frac{\bar{T}_w - T_r}{u_\infty}, \quad -\frac{1}{2} \frac{\text{Pr}^*}{C_p} = \frac{T_\infty - T_r}{u_\infty^2}. \quad (23)$$

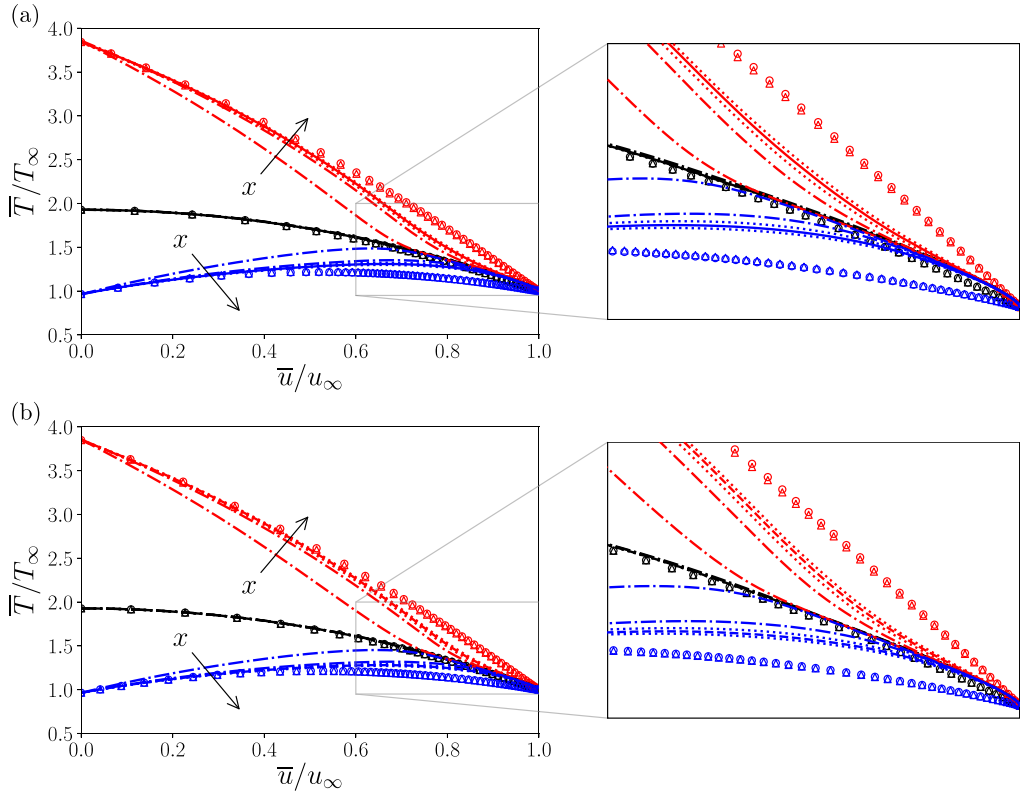


FIG. 4. Temperature-velocity profiles compared with Walz's equation. (a) Ideal gas cases; (b) constant Re_τ^* cases. Solid lines and dashed lines as in Table I. Dashed-dotted lines, the profiles at $x/\delta_{in} = 10, 20$; dotted lines, the profiles at $x/\delta_{in} = 28, 38$. Black solid, dashed-dotted, and dotted lines overlap each other. Circles, Walz's equation; triangles, Zhang's equation [15]. Circles and triangles almost overlap each other.

Finally, Walz's equation (15) may be derived by substituting the relations Eq. (23) to Eq. (21). Figure 4 shows the comparisons between the temperature-velocity profiles obtained by the present LES and Walz's equation. It is observed that all the present LES at $\bar{u}/u_\infty \lesssim 0.5$ converge to Walz's equation by increasing the streamwise location x , whereas the AD and ADcRe cases show a good agreement throughout the boundary layers (a similar result is also found in Ref. [34]). This suggests that the temperature field is sufficiently developed by the present LES at $x/\delta_{in} \gtrsim 28$. We note that, in the heated (red lines) and cooled (blue lines) wall cases, there are clear deviations between the present data and Walz's equation in the velocity range corresponding to the outer boundary layer regions, $\bar{u}/u_\infty \gtrsim 0.6$. In prior studies [34,44], similar discrepancies are also observed for wall-heated or -cooled turbulent boundary layers, and they concluded that the discrepancies originate from the step change of wall temperature. In this study, we revisit the discrepancies in the outer layer of the boundary layers with heated/cooled walls by analyzing the temperature-velocity equation in the following.

To understand the discrepancies from Walz's equation observed by the cases with wall heat transfer and also the good match throughout the boundary layers between the adiabatic cases and Walz's equation, we examine the two main assumptions used in the derivations of Walz's equation, i.e., equilibrium boundary assumptions (parallel flow and no pressure gradient assumptions) in the total energy equation in Eq. (16) and the momentum equation in Eq. (19). Assuming a statistically steady 2D flow (such as flat-plate boundary layers) and averaging in time and the homogeneous

spanwise direction, integrating the total energy equation in the wall-normal direction gives

$$\int_0^y \frac{\partial(\overline{\rho E})}{\partial t} = - \int_0^y \frac{\partial}{\partial x_j} \{ \overline{\rho E u_j} + \overline{p u_j} + \overline{q_j} - \overline{u_i \tau_{ij}} \} dy = 0, \quad (24)$$

and then

$$- \int_0^y \frac{\partial}{\partial x_j} \left\{ \frac{1}{2} \overline{\rho u_i u_i u_j} + \overline{\rho u_j h} + \overline{q_j} - \overline{u_i \tau_{ij}} \right\} dy = 0, \quad (25)$$

where the enthalpy $h = e + p/\rho = \gamma p/\rho(\gamma - 1)$. Taking the Reynolds and Favre decomposition and dividing into the wall-normal (y) and streamwise (x) components, Eq. (25) is represented as

$$\begin{aligned} & -\frac{1}{2} \overline{\rho \tilde{u}_i \tilde{u}_i \tilde{v}} - \frac{1}{2} \overline{\rho u_i' u_i' \tilde{v}} - \overline{\rho \tilde{u}_i u_i' v''} - \frac{1}{2} \overline{\rho u_i' u_i' v''} \\ & - \overline{\rho \tilde{v} \tilde{h}} - \overline{\rho v'' h''} - \overline{q_y} + \overline{q_w} + \overline{\tilde{u}_i \tau_{iy}} + \overline{u_i' \tau_{iy}} + \overline{u_i' \tau_{iy}'} \\ & - \int_0^y \frac{\partial}{\partial x} \left\{ \frac{1}{2} \overline{\rho \tilde{u}_i \tilde{u}_i \tilde{u}} + \frac{1}{2} \overline{\rho u_i' u_i' \tilde{u}} + \overline{\rho \tilde{u}_i u_i' u''} + \frac{1}{2} \overline{\rho u_i' u_i' u''} \right. \\ & \left. + \overline{\rho \tilde{u} \tilde{h}} + \overline{\rho u'' h''} + \overline{q_x} - \overline{\tilde{u}_i \tau_{ix}} - \overline{u_i' \tau_{ix}} - \overline{u_i' \tau_{ix}'} \right\} dy = 0. \end{aligned} \quad (26)$$

Finally, the wall-normal integrated total energy equation can be arranged as

$$\underbrace{\tilde{u} \overline{\mu} \frac{d\tilde{u}}{dy}}_{\text{term 1}} - \underbrace{\overline{\rho \tilde{u} u_i' \tilde{v}}}_{\text{term 2}} + C_p \underbrace{\frac{\overline{\mu}}{\text{Pr}} \frac{d\overline{T}}{dy}}_{\text{term 3}} + \underbrace{\overline{q_w}}_{\text{term 4}} - \underbrace{\overline{\rho v'' h''}}_{\text{term 5}} + \underbrace{\text{nonequilibrium terms}}_{\text{term 6}} = 0, \quad (27)$$

where $\overline{\tau_{xy}} \simeq \overline{\mu}(d\tilde{u}/dy)$, $\overline{q_y} = -C_p(\overline{\mu}/\text{Pr})(d\overline{T}/dy)$, and the term 6,

$$\begin{aligned} \text{nonequilibrium terms} &= -\frac{1}{2} \overline{\rho \tilde{u}_i \tilde{u}_i \tilde{v}} - \frac{1}{2} \overline{\rho u_i' u_i' \tilde{v}} - \overline{\rho \tilde{v} v'' v''} - \frac{1}{2} \overline{\rho u_i' u_i' v''} \\ & - \overline{\rho \tilde{v} \tilde{h}} + \overline{\tilde{v} \tau_{yy}} + \overline{u_i' \tau_{iy}} + \overline{u_i' \tau_{iy}'} \\ & - \int_0^y \frac{\partial}{\partial x} \left\{ \frac{1}{2} \overline{\rho \tilde{u}_i \tilde{u}_i \tilde{u}} + \frac{1}{2} \overline{\rho u_i' u_i' \tilde{u}} + \overline{\rho \tilde{u}_i u_i' u''} + \frac{1}{2} \overline{\rho u_i' u_i' u''} \right. \\ & \left. + \overline{\rho \tilde{u} \tilde{h}} + \overline{\rho u'' h''} + \overline{q_x} - \overline{\tilde{u}_i \tau_{ix}} - \overline{u_i' \tau_{ix}} - \overline{u_i' \tau_{ix}'} \right\} dy. \end{aligned} \quad (28)$$

The first five terms in Eq. (27) correspond to the integrated total energy equation under the equilibrium boundary layer assumptions, which are the same as Eq. (16), the origin of the derivation of Walz's equation. This indicates that the nonequilibrium terms in Eq. (28) are neglected in Walz's equation. We note that the nonequilibrium terms usually become dominant in outer boundary layer regions. First, we address the reason for the agreement between the adiabatic cases and Walz's equation throughout the boundary layers, although the nonequilibrium terms (which are neglected in the derivation of Walz's equation) are not negligible in the outer layer of the boundary layers. Figure 5 shows the profiles of each term of the integrated total energy equation in Eq. (27). The sum of the first five terms is represented as black lines. If the sum (black line in Fig. 5) is zero, it indicates that Eq. (16), which is the basis of Walz's equation, is satisfied. In the adiabatic cases, the viscous diffusion (term 1, red lines) and the local heat flux (term 3, blue lines), and the turbulent diffusion (term 2, orange lines) and the turbulent heat flux (term 5, cyan lines) are balanced, respectively. As for the nonequilibrium terms (term 6, gray dashed lines), although each of the terms shown in Eq. (28) has a non-negligible value in the outer-layer regions (although not shown individually in the figure), they almost cancel each other out. As a result, the sum of the nonequilibrium terms becomes

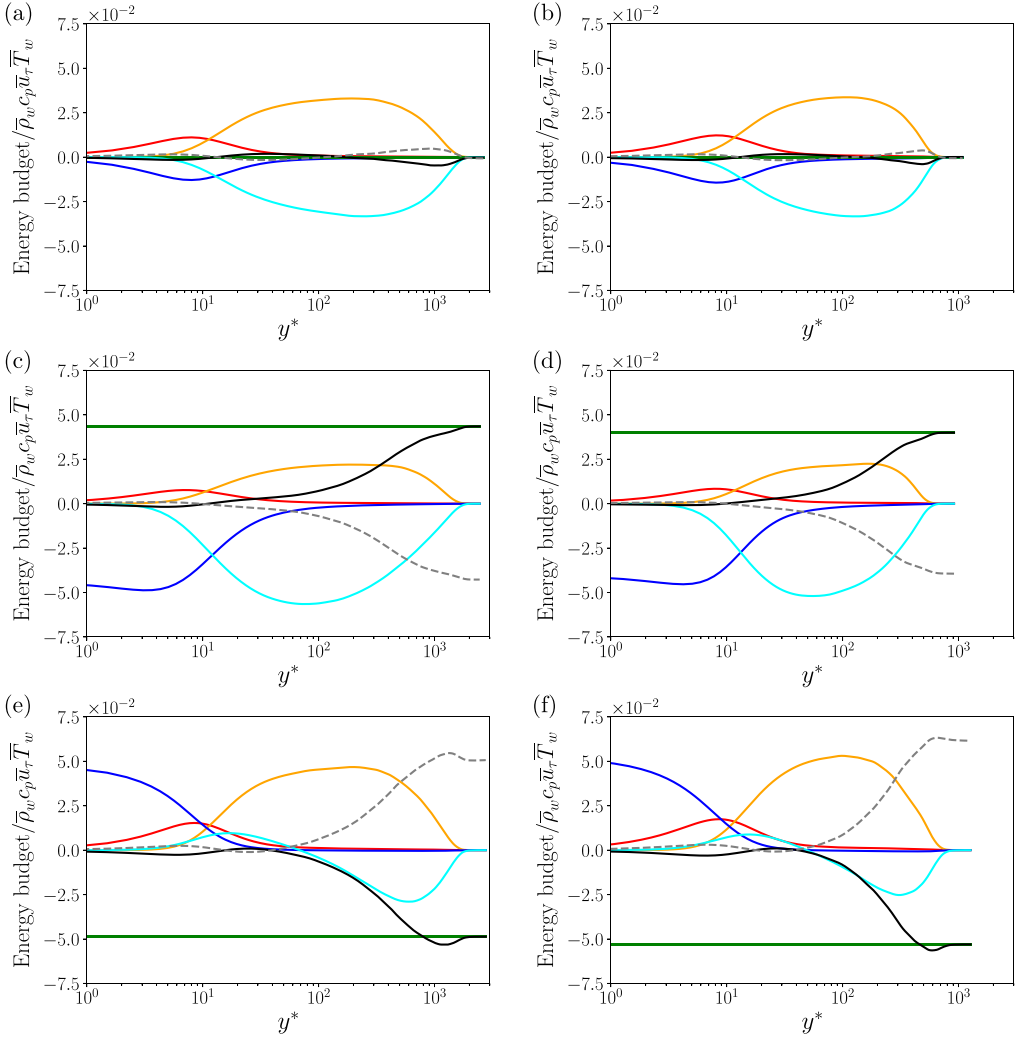


FIG. 5. Profiles of the components of the integrated energy equation shown in Eq. (27). (a) AD, (b) ADcRe, (c) HE, (d) HEcRe, (e) CO, and (f) COcRe. Red lines, term 1; orange lines, term 2; blue lines, term 3; green lines, term 4; cyan lines, term 5; black lines, sum from term 1 to term 5; gray dashed lines, term 6.

almost zero throughout the adiabatic boundary layers, which means that the assumption of Eq. (16) is satisfied even in the outer layer of the boundary layers. Furthermore, related to the equilibrium assumption for the momentum equation, when the wall heat flux \bar{q}_w is zero (i.e., $\bar{T}_w \approx T_r$), the right-hand side of Eq. (20), which includes the wall shear stress $\bar{\tau}_w$ approximated by the momentum balance Eq. (19) for equilibrium boundary layers, becomes zero. Therefore, the induced errors from the equilibrium boundary layer assumption in the total shear stress balance equation do not need to be included in the adiabatic cases. As a result, the adiabatic cases collapse with Walz's equation throughout the boundary layers.

On the other hand, for the heated and cooled cases, the wall heat flux is either positive or negative, and a balance of the viscous diffusion, local heat flux, turbulent diffusion, and the turbulent heat flux cannot be achieved as shown in Fig. 5. In the outer-layer region, the sum of the first five terms in Eq. (28) converges to the wall heat flux, because these terms, except for the wall heat flux,

become zero at the outer layer of the boundary layer. Furthermore, in the outer-layer region, the heated and cooled cases do not satisfy the equilibrium boundary layer assumptions and thus the total shear stress balance Eq. (19) is not valid (as will be shown in Fig. 7). The results indicate that the equilibrium boundary layer assumptions in Eqs. (16) and (19), and thus the results of Walz's equation, cannot be applied in the outer boundary layer regions for the heated and cooled cases. The analyses indicate that Walz's equation, and similarly formulated temperature-velocity relationships [4,15], is not applicable to represent the correct temperature-velocity relations for the cases with wall heat transfer in outer boundary layer regions, since the effects of the nonequilibrium terms in the outer-layer region [i.e., the terms shown in Eq. (28)] cannot be neglected. Note that a more detailed analysis of the nonequilibrium terms is shown in Appendix A.

To conclude, the spatially developed temperature and velocity fields obtained by the present LES are sufficiently developed at $x/\delta_{in} \gtrsim 28$. The discrepancies between the LES and Walz's equation in the outer layer are not due to the insufficient streamwise length from the heated/cooled switching point but due to the nonequilibrium boundary layer's effects that are neglected in Walz's equation. On the other hand, the good agreement in the adiabatic cases throughout the boundary layers is that the nonequilibrium effects are canceled out with each other, resulting in the validity of Walz's equation throughout the boundary layers.

B. Mean velocity profiles

Figure 6 shows several mean-velocity scales, namely \bar{u}/u_∞ , \bar{u}^+ , \bar{u}_{vD}^+ , and \bar{u}^* , which are defined as

$$\bar{u}^+ = \frac{\bar{u}}{\bar{u}_\tau}, \quad (29)$$

$$\bar{u}_{vD}^+ = \int_0^{\bar{u}^+} \sqrt{\frac{\bar{\rho}}{\bar{\rho}_w}} d\bar{u}^+, \quad (30)$$

$$\bar{u}^* = \int_0^{\bar{u}_{vD}^+} \left(1 + \frac{y}{\text{Re}_\tau^*} \frac{d \text{Re}_\tau^*}{dy}\right) d\bar{u}_{vD}^+ = \int_0^{\bar{u}^+} \left(\frac{\bar{\rho}}{\bar{\rho}_w}\right)^{1/2} \left(1 + \frac{1}{2} \frac{y}{\bar{\rho}} \frac{d\bar{\rho}}{dy} - \frac{y}{\bar{\mu}} \frac{d\bar{\mu}}{dy}\right) d\bar{u}^+, \quad (31)$$

where $\bar{u}_\tau = \sqrt{\bar{\tau}_w/\bar{\rho}_w}$ is the friction velocity, y is the wall-normal coordinate, and Re_τ^* is the semi-local Reynolds number defined in Eq. (11). Each of these transformations is capable of collapsing mean velocity profiles for certain cases, e.g., \bar{u}^+ for isothermal (incompressible) flows, \bar{u}_{vD}^+ for adiabatic compressible flows, and \bar{u}^* for compressible flows involving wall heat transfer [22,23], while none of these mean-velocity scales collapse all the cases to the incompressible law of the wall. Note that \bar{u}^* can be given with two expressions as shown in Eq. (31): the first expression is based on the function of the semi-local Reynolds number as proposed by Patel *et al.* [23] and the second expression was proposed by Trettel and Larsson [22]. While both expressions are mathematically equivalent, we will use the first expression in our later discussions. Also, we note that \bar{u}_{vD}^+ and \bar{u}^* are equivalent for the constant Re_τ^* cases, since $d \text{Re}_\tau^*/dy = 0$, and also the semi-local wall distance $y^* = \sqrt{\bar{\rho}}\sqrt{\bar{\tau}_w}y/\bar{\mu}$ is identical to the wall coordinate $y^+ = \sqrt{\bar{\rho}_w}\sqrt{\bar{\tau}_w}y/\mu_w$, because of Eq. (12).

As expected, the \bar{u}/u_∞ velocity profiles show different trends with respect to changes in wall temperature for the ideal gas and the constant Re_τ^* cases in Figs. 6(a) and 6(b). The ideal gas cases show differences mainly for $y/\delta_{99} < 0.1$, where it can be seen that the higher the wall temperature, the lower the near-wall velocity gradients. On the other hand, the constant Re_τ^* cases show larger differences around $y/\delta_{99} \approx 0.2$, where the highest velocity is obtained for the heated case. Compared to the incompressible velocity profiles, all the cases show a higher velocity for $y/\delta_{99} > 0.1$. Qualitatively similar observations are also reported in Ref. [45]. The \bar{u}^+ profiles are shown in Fig. 6(c). Almost all the compressible cases show large deviations from the incompressible law of the wall, and the trends are similar for the cases with the same wall temperature; e.g., the HE and HEcRe case are below the incompressible law of the wall. The van Driest transformed velocity

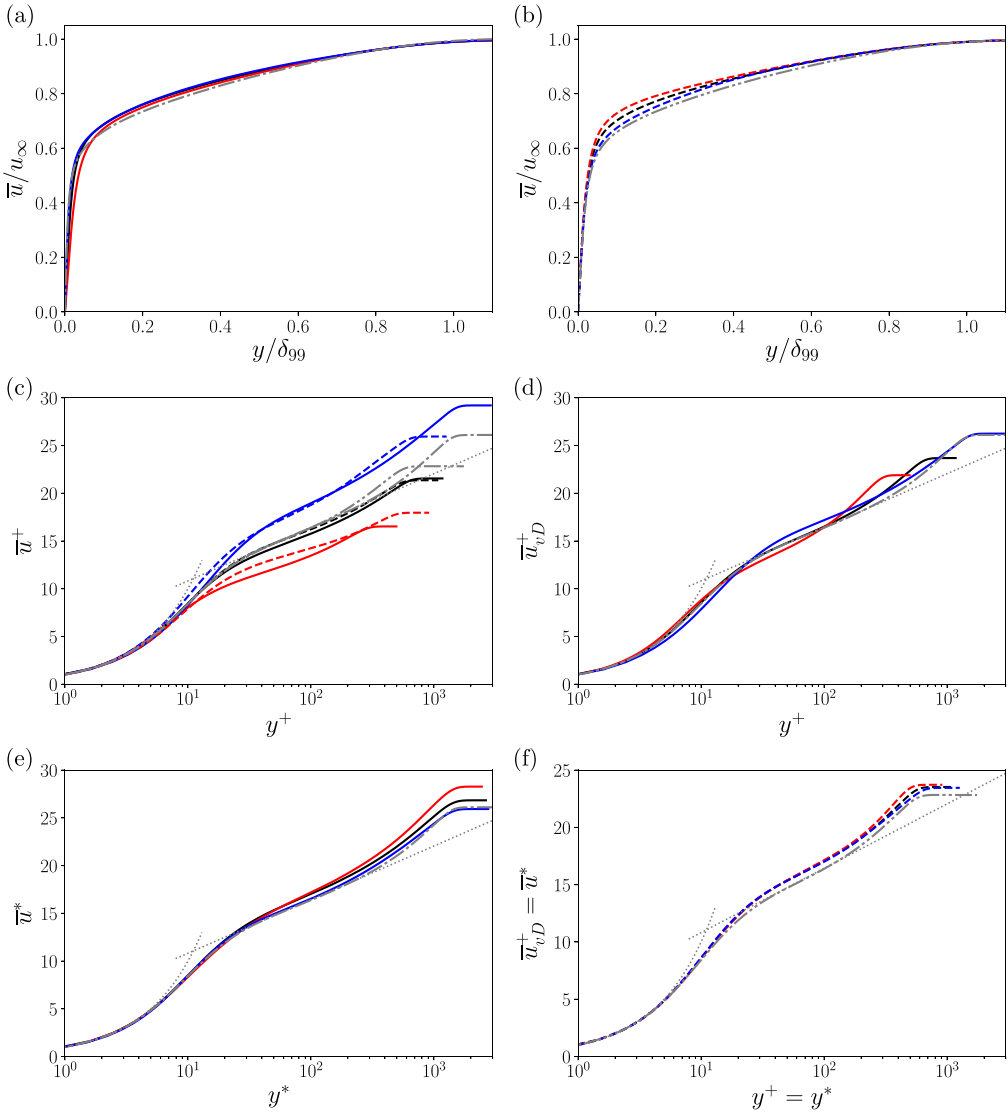


FIG. 6. Distributions of streamwise mean-velocity \bar{u} . (a), (b) Mean velocity normalized by the freestream value [(a) ideal gas cases; (b) constant Re_τ^* cases], (c) mean velocity normalized by the friction velocity, (d) van Driest transformed velocity, and (e), (f) transformed velocity based on semi-local scaling [22,23] [(e) ideal gas cases; (f) constant Re_τ^* cases]. Gray dotted lines, incompressible law of the wall [$y^+ = u^+$ and $y^+ = \ln(u^+)/0.41 + 5.2$]; other lines, as in Table I.

\bar{u}_{vD}^+ is shown in Fig. 6(d), which is known to collapse adiabatic compressible boundary layer flows with ideal gases to the incompressible law of the wall. However, both the heated and cooled case show disagreements with the adiabatic case, which clearly suggests that the wall heat flux must be considered for the van Driest velocity scaling [7,16,29]. Figures 6(e) and 6(f) show the velocity transformation \bar{u}^* proposed by Trettel and Larsson [22] and Patel *et al.* [23]. Figure 6(e) shows small deviations among the three ideal gas cases compared with \bar{u}^+ in Fig. 6(c) or \bar{u}_{vD}^+ in Fig. 6(d), although there is a slight offset in the log-layer regions, which is larger in the heated case and

smaller in the cooled case. Similar tendencies for isothermal boundary layer cases are also observed in other work [46]. On the other hand, the constant Re_τ^* cases are in good agreement with each other from the wall to the log layer, but again with a slight log-law offset, shown in Fig. 6(f). Also, some deviations are observed in the wake region between the compressible and incompressible cases, which are larger in the compressible cases and smaller in the incompressible one. The reason behind the collapsed mean velocity in Fig. 6(f) and the discussions on how the constant semi-local Reynolds number affects the transformed mean-velocity profiles are provided in Appendix B.

In summary, two conclusions can be made. First, the van Driest velocity transformation appears to overlap with the incompressible law of the wall, only in the limit of ideal gas flows over adiabatic walls. For nonideal gases, such as for the constant Re_τ^* cases with an adiabatic wall [Fig. 6(f)] or for ideal gas flows with wall heat transfer [Fig. 6(d)], no collapse with the incompressible law is observed. Second, the \bar{u}^* transformation is capable of collapsing the velocity profiles, irrespective of adiabatic, heated or cooled walls, or ideal and nonideal gases. For the ideal gas cases, the deviations in the viscous sublayer and the log layer become smaller compared with the van Driest transformation; however, the observed deviations have a significant physical meaning which is related to changes in near-wall turbulence structures, as we will discuss later. Moreover, a log-law offset is observed for all \bar{u}^* profiles with respect to the incompressible case [e.g., see colored dashed lines and gray dot-dot-dashed line in Fig. 6(f)]. This suggests a Mach number effect, which must be taken into account; see, for example, work by Zhang *et al.* [21].

C. Relation between transformed velocity \bar{u}^* and viscous stress

We saw in Sec. IV B that \bar{u}^* shows a slightly higher log law for all the cases if compared to the incompressible cases. In this section, the derivation of the velocity transformation \bar{u}^* is summarized in detail, and a clear connection between \bar{u}^* and the viscous stress is established.

The \bar{u}^* velocity transformation is derived from the viscous stress $\bar{\tau}_{xy}/\bar{\tau}_w$, based on the observation that $\bar{\tau}_{xy}/\bar{\tau}_w$ collapses for turbulent channel flows with arbitrary density and dynamic viscosity variations [23]. The viscous stress is defined as a product of dynamic viscosity and streamwise velocity gradient as

$$\frac{\bar{\tau}_{xy}}{\bar{\tau}_w} = \frac{\overline{\mu \frac{du}{dy}}}{\bar{\tau}_w} \approx \frac{\bar{\mu} \frac{d\bar{u}}{dy}}{\bar{\tau}_w}. \quad (32)$$

Equation (32) can be replaced with a formulation used semi-local Reynolds number Re_τ^* and transformed velocity \bar{u}_{vD}^+ as

$$\frac{\bar{\mu} \frac{d\bar{u}}{dy}}{\bar{\tau}_w} = \frac{\delta_{99}}{\text{Re}_\tau^*} \frac{\bar{\mu}}{\bar{\mu}_w} \frac{d\bar{u}^+}{dy} = \frac{\delta_{99}}{\text{Re}_\tau^*} \frac{d\bar{u}_{vD}^+}{dy}. \quad (33)$$

Using the chain rule, the velocity gradient in Eq. (33) can be expanded as $d\bar{u}_{vD}^+/dy = (dy^*/dy)d\bar{u}_{vD}^+/dy^*$. Thus we can rewrite Eq. (33) as

$$\frac{\delta_{99}}{\text{Re}_\tau^*} \frac{d\bar{u}_{vD}^+}{dy} = \frac{\delta_{99}}{\text{Re}_\tau^*} \frac{dy^*}{dy} \frac{d\bar{u}_{vD}^+}{dy^*}. \quad (34)$$

Here, the semi-local length scale $y^* = \text{Re}_\tau^* y / \delta_{99}$, and thus dy^*/dy can be expanded by using the Leibniz rule as

$$\frac{\delta_{99}}{\text{Re}_\tau^*} \frac{dy^*}{dy} \frac{d\bar{u}_{vD}^+}{dy^*} = \frac{\delta_{99}}{\text{Re}_\tau^*} \left(\frac{dy}{dy} \frac{\text{Re}_\tau^*}{\delta_{99}} + \frac{d\text{Re}_\tau^*}{dy} \frac{y}{\delta_{99}} \right) \frac{d\bar{u}_{vD}^+}{dy^*}. \quad (35)$$

Summarizing the above equations [from Eq. (32) to Eq. (35)], a relationship between the viscous stress and the formulation of \bar{u}^* is shown as

$$\frac{\bar{\tau}_{xy}}{\bar{\tau}_w} = \frac{\overline{\mu \frac{du}{dy}}}{\bar{\tau}_w} \approx \frac{\bar{\mu} \frac{d\bar{u}}{dy}}{\bar{\tau}_w} = \left(1 + \frac{y}{\text{Re}_\tau^*} \frac{d \text{Re}_\tau^*}{dy}\right) \frac{d\bar{u}_{vD}^+}{dy^*} = \frac{d\bar{u}^*}{dy^*}. \quad (36)$$

After all, transformed velocity \bar{u}^* can be approximated as

$$\bar{u}^* \approx \int_0^{y^*} \frac{\bar{\tau}_{xy}}{\bar{\tau}_w} dy^*, \quad (37)$$

and Eq. (37) suggests that the viscous stress profile affects the disagreement in \bar{u}^* directly. In the next subsection, the viscous stress will be shown with the streamwise total shear stress balance, which explains the log-law offset of \bar{u}^* in Fig. 6.

D. Streamwise momentum balance

For a developing turbulent boundary layer flow, the streamwise stress balance equation can be written as

$$-\int_0^y \left(\frac{d\bar{p}}{dx}\right) dy - \int_0^y \left(\bar{\rho}u \frac{\partial \tilde{u}}{\partial x} + \bar{\rho}v \frac{\partial \tilde{u}}{\partial y}\right) dy - \bar{\rho}u''v'' + \bar{\tau}_{xy} \approx \bar{\tau}_w, \quad (38)$$

where the terms from left to right correspond to the pressure gradient, the convection, the Reynolds shear stress, and the viscous stress. We now investigate this stress balance equation to understand the differences between the ideal gas and constant Re_τ^* cases more clearly. Figure 7 shows the profiles of each term in Eq. (38), normalized by the total shear stress $\bar{\tau}_w$. Figures 7(a) and 7(b) show the viscous stress profiles, and some small deviations among the ideal gas cases can be observed in the left figure. On the other hand, in the right figure for the constant Re_τ^* cases, a very good agreement among the compressible cases is seen, but with a slight offset compared to the incompressible case, similar to what is observed for the transformed velocity \bar{u}^* in Fig. 6(f). Also, the primary differences of the viscous stress profiles for the ideal gas cases are observed at $y^* \lesssim 100$. Therefore, the discussions hereafter are focused on the range of $y^* \lesssim 100$.

In Figs. 7(c) and 7(d), the pressure term shows very small contributions (for $y^* \lesssim 100$) for all the cases, which suggests that it can be ignored in the stress balance for all the present cases. Also, for the convective terms in Figs. 7(e) and 7(f), all of the compressible cases show a comparable value to the incompressible case (i.e., around 0.1 or less), which can be considered as negligible for the inner-layer stress balance. In contrast to the pressure and convection terms, the Reynolds shear stress term, shown in Figs. 7(g) and 7(h), has a dominant contribution in the inner layer for all the cases. The viscous stress and the Reynolds stress balance each other in the viscous- and log-layer regions given the equilibrium boundary layer assumption, as Eq. (19). The variations in the Reynolds stress profiles, for example, among the three ideal gas cases in Fig. 7(e), or between constant Re_τ^* and incompressible cases in Fig. 7(f), are directly connected to the variations in the viscous stress profiles shown in Figs. 7(a) and 7(b). Judging from this similar behavior of the Reynolds and viscous stress profiles, the Reynolds stresses are thus related with the viscous stresses and affect the disagreement of the transformed velocity \bar{u}^* profiles. The difference in the Reynolds stress profiles indicates the change of near-wall turbulent structures, which is considered to be caused by the changes in the semi-local Reynolds number. Therefore, the turbulent physics corresponding to the stress balance changes will be analyzed in Sec. IV E.

E. Near-wall turbulent structures

The Reynolds stress, discussed in Sec. IV D, is a result of the turbulent physics in boundary layers, and changes in Reynolds stress indicate directly some form of changes in near-wall turbulent

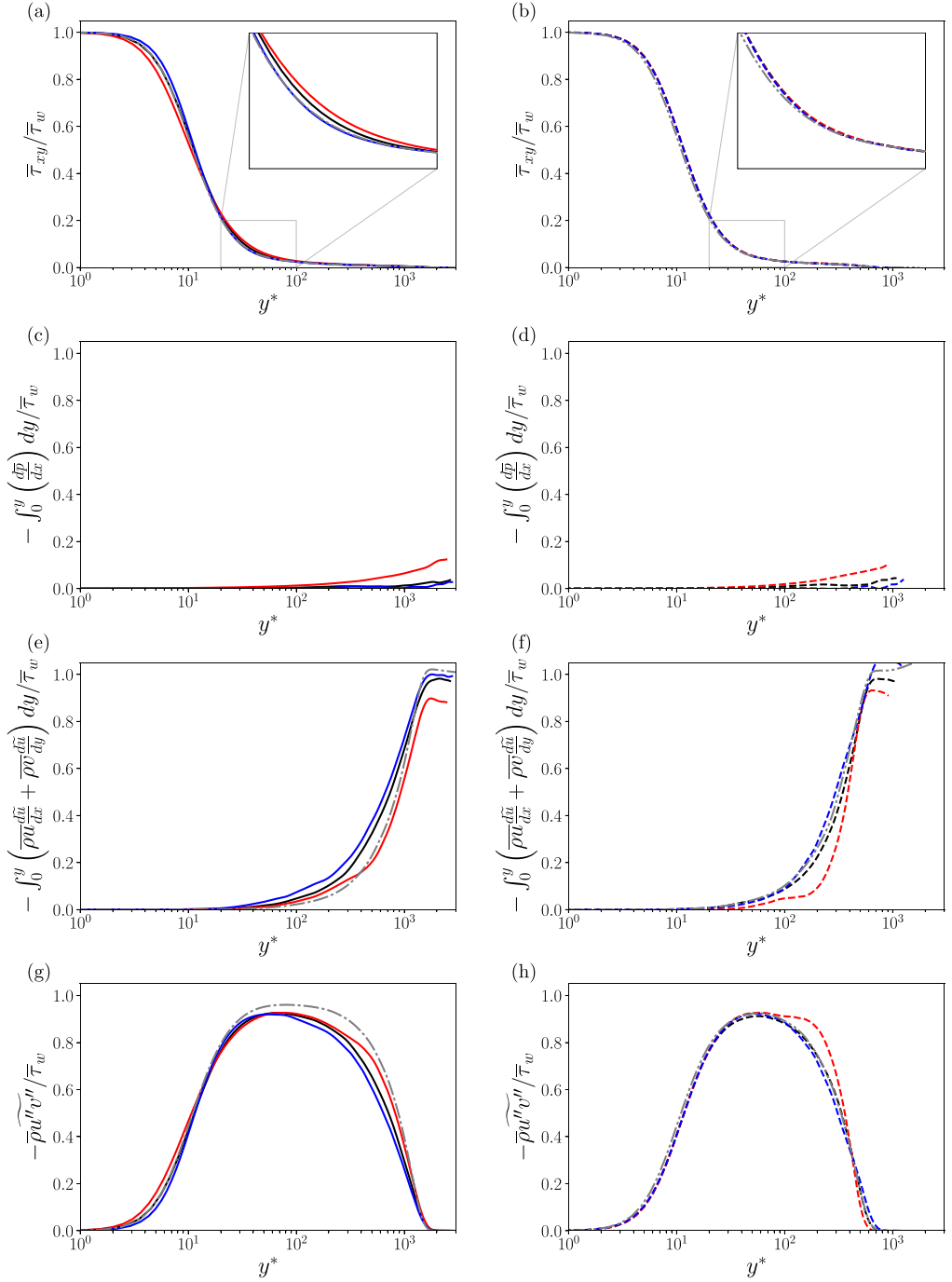


FIG. 7. Wall-normal distributions of each term in the streamwise stress balance equation (38). (a), (b) Viscous term; (c), (d) pressure term; (e), (f) convective term; (g), (h) Reynolds shear stress term. Left column, ideal gas cases; right column, constant Re_τ^* cases. Lines as in Table I.

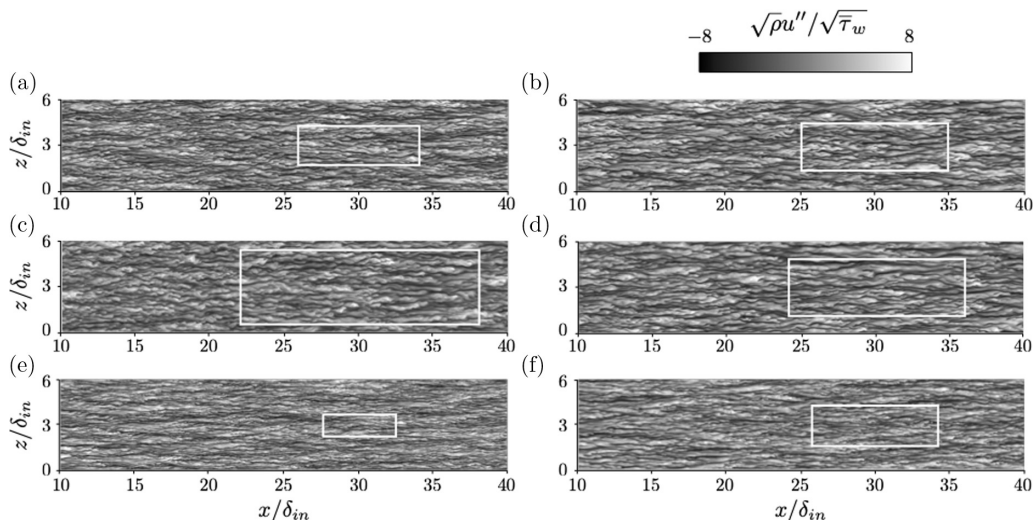


FIG. 8. Instantaneous streamwise velocity fluctuations $\sqrt{\rho}u''/\sqrt{\tau_w}$ on (x, z) plane at $y^* \simeq 15$ using x - z coordinates. White boxes with the size of $L_{x^*} = 3500$ and $L_{z^*} = 1000$, where $L_{x^*} = \sqrt{\rho}\sqrt{\tau_w}L_x/\bar{\mu}$ and $L_{z^*} = \sqrt{\rho}\sqrt{\tau_w}L_z/\bar{\mu}$ are semi-local inner-layer length scales. Left column, ideal gas cases; right column, constant Re_τ^* cases. (a) AD, (b) ADcRe, (c) HE, (d) HEcRe, (e) CO, and (f) COcRe.

structures. Because of this, we now discuss near-wall turbulent structures for all the compressible cases to quantify the influences of thermophysical property variations.

Figure 8 shows the instantaneous streamwise velocity fluctuations at $y^* \simeq 15$ to give an impression of the near-wall turbulent structures. Near-wall, low-speed streaks and high-speed streaks are visualized as black and white streamwisely elongated structures [47]. The ideal gas cases (left column) indicate larger turbulent length scales for the heated case [Fig. 8(c)], while they are smaller for the cooled one [Fig. 8(e)], if compared to the simulation with the adiabatic boundary condition [Fig. 8(a)]. To some extent, a similar behavior can be seen for the constant Re_τ^* cases (right column) in Figs. 8(b), 8(d), and 8(f), which show the quasiadiabatic, heated, and cooled cases, respectively. It is important to note that the turbulent structures in Fig. 8 are plotted as a function of outer-layer length scales in relation to the boundary layer thickness δ_{in} . Therefore, the apparent changes in size of the turbulent structures can be associated to changes in local Reynolds number at the wall-parallel planes displayed in these figures.

To substantiate the previous statement, Fig. 9 shows the turbulent structures as a function of the inner-layer length scale defined by y^* . Note that the domains of the contour plots in Fig. 9 correspond to the white boxes shown in Fig. 8, which all have the same size in terms of semi-local (inner-layer) length scales $l_v^* = \bar{\mu}/(\sqrt{\rho}\sqrt{\tau_w})$. Regarding the ideal gas cases (left column), the heated case [Fig. 9(c)] shows smaller structures and the cooled case [Fig. 9(e)] shows larger ones, opposite to what has been observed in Fig. 8. Note that the tendency of the ideal gas cases shown in Fig. 9 is similar to the results in Ref. [7] that are obtained with several wall temperature cases having an almost same value of the friction Reynolds number. On the other hand, the constant Re_τ^* cases (right column) seem to have the same turbulent length scales independent of adiabatic, heated, and cooled walls. Further, the differences between the ideal gas cases and the constant Re_τ^* cases in Fig. 9 are consistent with the Reynolds stress profiles shown in Fig. 7: a larger difference in ideal gas cases and a good agreement among the constant Re_τ^* cases. Quantitative comparisons of turbulent structures are shown in Fig. 10 as spanwise correlations. Figures 10(a) and 10(b) correspond to Figs. 8 and 9, respectively, and the changes in turbulent length scale between the different wall temperature cases are consistent between the instantaneous and statistical results. In Fig. 10(a),

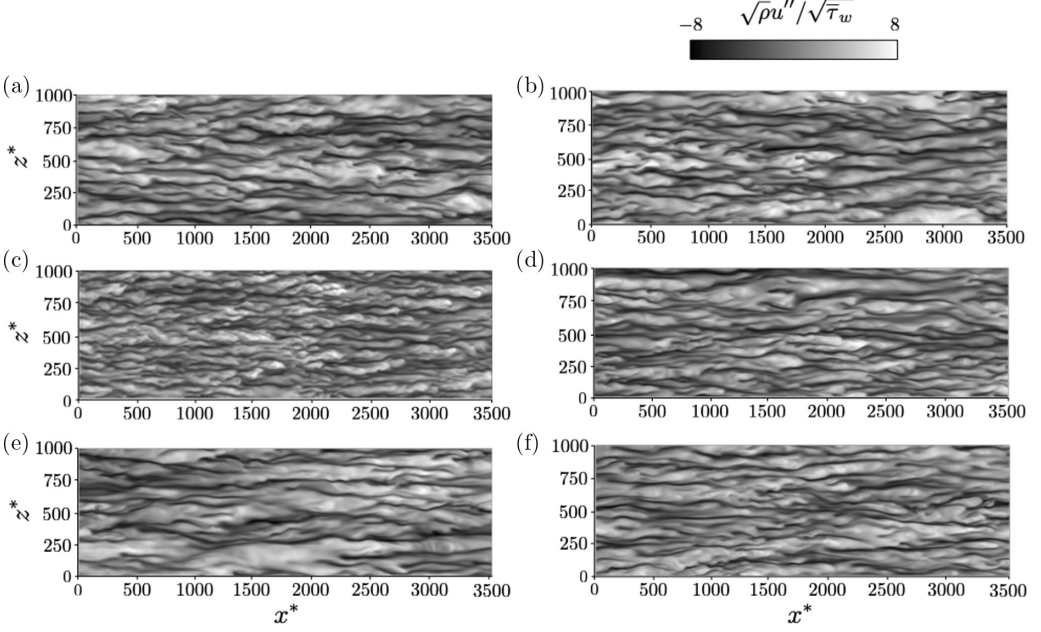


FIG. 9. Instantaneous streamwise velocity fluctuations $\sqrt{\rho}u''/\sqrt{\tau_w}$ on (x, z) plane at $y^* \simeq 15$ using x^* - z^* coordinates (extracted white box as in Fig. 8). Left column, ideal gas cases; right column, constant Re_τ^* cases. (a) AD, (b) ADcRe, (c) HE, (d) HEcRe, (e) CO, and (f) COcRe.

which is scaled by the outer-layer length δ_{99} , a distance to a zero-correlation point becomes larger in the heated cases and smaller in the cooled cases. On the other hand, in Fig. 10(b), which is scaled by semi-local length l_v^* , the zero-correlation points become closer to each other, while the length scale of the cooled ideal gas case becomes larger and the heated ideal gas case becomes smaller, opposite to Fig. 10(a). In the constant Re_τ^* cases, the correlation profiles collapse well with each other in Fig. 10(b), just as shown in Fig. 9. The results shown in Figs. 9 and 10(b) indicate the importance of the semi-local Reynolds number on the scaling turbulent structures, regardless of the distributions of thermodynamic properties, such as temperature, density, or viscosity, between the cases. We

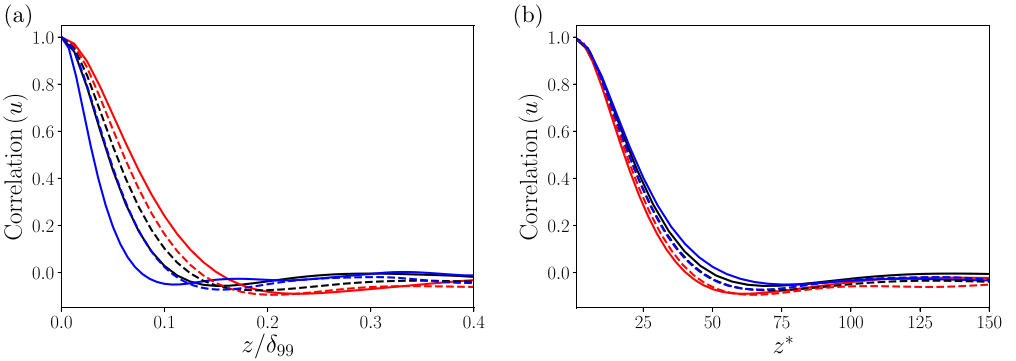


FIG. 10. Distributions of two-point correlations of streamwise velocity at $y^* \approx 15$. (a) Outer-layer length scale; (b) semi-local (inner-layer) length scale. Lines as in Table I. Black and blue dashed lines almost overlap each other in (b).

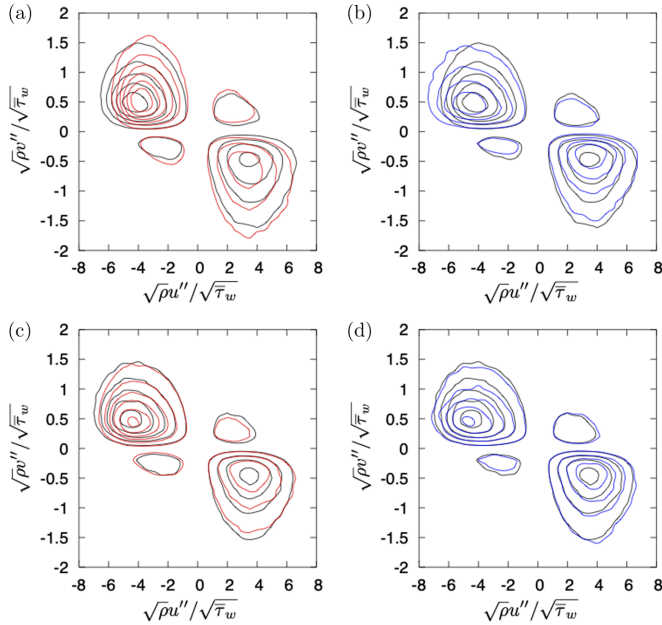


FIG. 11. Joint probability density function consisting of $\sqrt{\rho}u''/\sqrt{\tau_w}$ and $\sqrt{\rho}v''/\sqrt{\tau_w}$ at $y^* \simeq 15$. (a) HE and (b) CO, compared with AD. (c) HEcRe and (d) COcRe, compared with ADcRe. Black, quasiadiabatic; red, heated; blue, cooled.

note that similar observations on the scaling of turbulent statistics and structures with respect to semi-local Reynolds number distributions are reported in prior studies. For example, Ref. [32] shows that the turbulent statistics can also be collapsed between cases with similar semi-local Reynolds number distributions in the wall-normal direction, not only for the cases with the constant semi-local Reynolds number. This clearly shows the appropriateness of the semi-local Reynolds number to characterize variable property flows.

To indicate the differences in the near-wall turbulent structures more clearly, weighted joint probability density functions (JPDF) consisting of streamwise and wall-normal velocity fluctuations ($\sqrt{\rho}u''/\sqrt{\tau_w}$ and $\sqrt{\rho}v''/\sqrt{\tau_w}$) at $y^* \simeq 15$ are shown in Fig. 11. The quadrant analysis decomposes the Reynolds shear stress into four events [48]: quadrant 1 (Q1) events have $u'' > 0$ and $v'' > 0$, Q2 events (called “ejection”) have $u'' < 0$ and $v'' > 0$, Q3 events have $u'' < 0$ and $v'' < 0$, and Q4 events (called “sweep”) have $u'' > 0$ and $v'' < 0$. Near-wall low-speed and high-speed streaks are associated with each Q2 ejection and Q4 sweep events, respectively. In the upper figures, which show the ideal gas cases, the adiabatic case (black contour lines) is compared to the heated (red contour lines) and cooled (blue contour lines) case, respectively. As can be seen, a decrease in $\sqrt{\rho}u''/\sqrt{\tau_w}$ and an increase in $\sqrt{\rho}v''/\sqrt{\tau_w}$ are observed in the Q2 and Q4 events for the heated case, while the opposite occurs for the cooled case. On the other hand, much smaller differences of the turbulent structures are seen for the constant Re_τ^* cases. The changes in JPDF in the ideal gas cases with heated/cooled walls and the agreement of JPDF obtained by the constant Re_τ^* cases are consistent with the observations for the turbulent length scale of the streaks in Fig. 9: the larger differences in the ideal gas cases and the similar ones in the constant Re_τ^* cases. Moreover, notable changes in the JPDF distributions occur in the Q2 ejection events for the ideal gas cases. Therefore, we focus on the Q2 ejection events and investigate the turbulent structures in more detail in the following discussion. The coherent turbulent structures are time and space dependent unsteady phenomena so that the conditional averaging process for capturing the instantaneous physics is needed to evaluate the features of the structures [49]. The conditionally averaged ejection

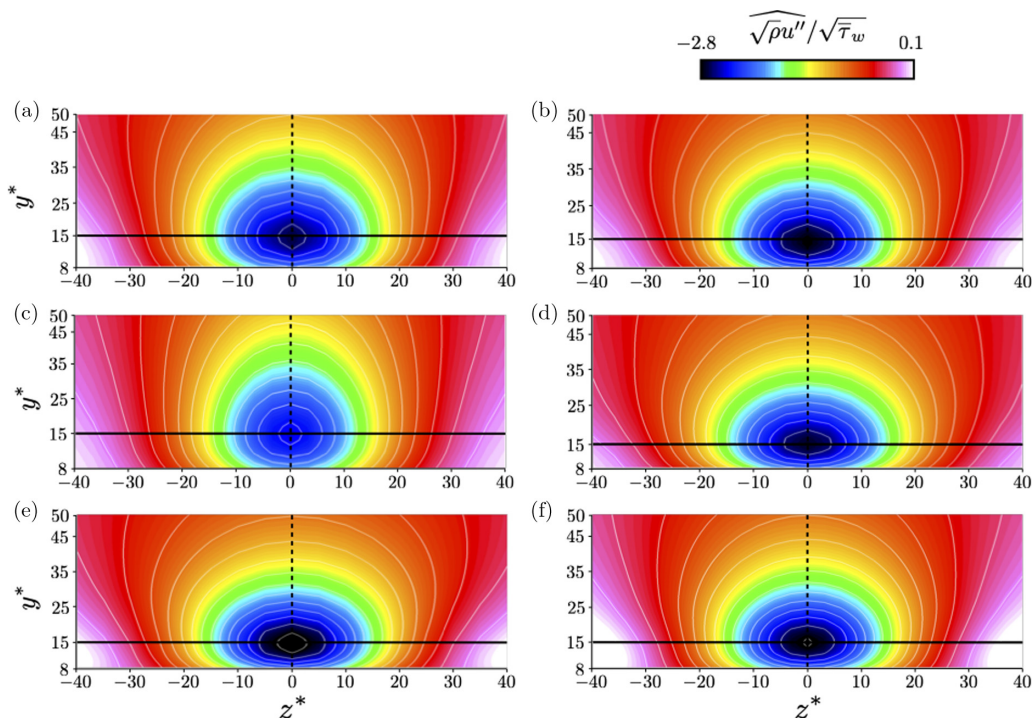


FIG. 12. Conditional averaged flow fields taken as identified by the Q2 conditions along $y^* \simeq 15$ (black solid lines). (a) AD, (b) ADcRe, (c) HE, (d) HEcRe, (e) CO, and (f) COcRe. Black solid lines, $y^* \simeq 15$; black dashed lines, spanwise center of the averaged domain.

phenomena, which are the dominant turbulent motions' near-wall regions of turbulent boundary layers, are obtained by taking conditional averages of streamwise velocity fluctuations, as identified by the Q2 ($u'' < 0$ and $v'' > 0$) conditions. The Q2 events are detected spanwisely along $y^* \simeq 15$ (black solid lines in Fig. 12), and the size of the averaging window for capturing low-speed streaks is $8 < y^* < 50$ in wall-normal and $L_{z^*} = 80$ in spanwise direction, respectively. Note that the hat $\widehat{\cdot}$ denotes time and spatial conditional averaged values. The center regions of $\widehat{\sqrt{\rho u''}} / \sqrt{\tau_w}$, which correspond to low-speed streak, are shown in Fig. 12. Clear differences can be seen. For the ideal gas cases (left column), stronger negative velocity fluctuations are observed for the cooled case, which is also confirmed in Fig. 11. The structures of the low-speed streak may be identified in Fig. 12. The low-speed streak is elongated in the wall-normal direction for the heated case and in the spanwise direction for the cooled case when compared to the adiabatic case. On the other hand, in the constant Re_τ^* cases (right column), both the strength of the negative velocity fluctuations and the structures are similar among the cases, and the characteristics are consistent with the results in Figs. 9 and 11. We note that the differences in mean wall-normal velocity distributions are observed in the same y^* range of Fig. 12, which is similar to the vertical changes of conditionally averaged turbulent structures among the different wall temperature cases: the greater the ejection height, the larger the mean wall-normal velocity. This indicates that the generation of the wall-normal velocity causes the vertical changes of turbulent structures.

Finally, the conditional-averaged velocity distributions and their wall-normal derivatives are shown in Fig. 13. The line plots are extracted from the black dashed lines in Fig. 12. In Fig. 13(a), the streamwise velocity fluctuations have a peak at $y^* \simeq 15$ in all the cases, which are corresponding to the low-speed streak shown in the center of Fig. 12. Figures 13(b) and 13(c) show the conditional-averaged velocity and its wall-normal derivative, respectively. The larger mean velocity

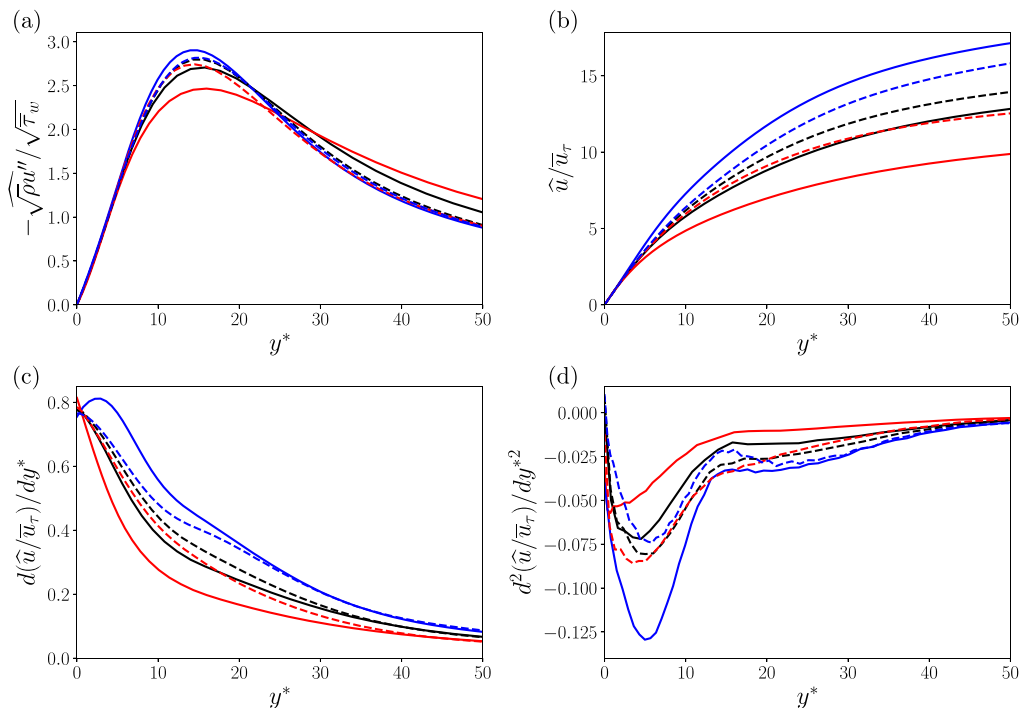


FIG. 13. Distributions of conditional averaged flow fields (profiles along dashed lines in Fig. 12). (a) Streamwise velocity fluctuations $\sqrt{\widehat{\rho u''}} / \sqrt{\overline{\tau}_w}$, (b) streamwise velocity $\widehat{u} / \overline{u}_\tau$, (c) wall-normal derivative of streamwise velocity $d(\widehat{u} / \overline{u}_\tau) / dy^*$, and (d) second derivative of streamwise velocity $d^2(\widehat{u} / \overline{u}_\tau) / dy^{*2}$. Lines as in Table I.

and wall-normal derivative are obtained by the cooled cases, and lower distributions are obtained by the heated cases, in both the ideal gas and constant Re_τ^* cases. The observed relationship between the wall-normal derivatives and the streamwise velocity fluctuations around $y^* \simeq 15$ (i.e., the larger the velocity gradient is, the stronger the velocity fluctuations occur) qualitatively follows a conventional gradient-diffusion hypothesis used frequently for turbulent diffusion modeling [50]. Also, compared with the ideal gas cases, the constant Re_τ^* cases show smaller deviations in Figs. 13(a), 13(b) and 13(c). The differences between the heated and cooled ideal gas cases and smaller deviations among the constant Re_τ^* cases are consistent in the results shown in Figs. 9, 11, and 12. Further, the second derivatives in Fig. 13(d) show a local maximum around $y^* \simeq 15$ and approach toward zero, where the peak of the velocity fluctuations is observed. Based on a streak instability as discussed in Refs. [51–53], the inflectional velocity distributions are considered to cause strong instabilities and breakdown of the low-speed streaks, which induce the large velocity fluctuations. To conclude, the results in Fig. 13 indicate a clear relationship between the velocity fluctuations and the mean velocity gradients.

V. CONCLUSIONS

In this paper, the effects of the semi-local Reynolds number in wall heated and cooled supersonic turbulent boundary layers were evaluated from the viewpoints of mean-velocity scaling laws, stress balance, and turbulent structures. Adiabatic, heated, and cooled wall turbulent boundary layer simulations have been performed at a Mach number of 2.28. In order to distinguish between Mach number and semi-local Reynolds number effects, in addition to the cases with the conventional

dynamic viscosity μ given by Sutherland's law (i.e., the semi-local Reynolds number Re_τ^* changes in wall-normal direction), we performed simulations for which the semi-local Reynolds number is constant in wall-normal direction. This is achieved by setting $\mu/\mu_w = \sqrt{\rho/\rho_w}$, whereby the semi-local Reynolds number is then constant.

One of the noticeable matters in this study is the effects of the semi-local Reynolds number. Regardless of the wall temperature (i.e., wall heat flux), the constant wall-normal profiles of the semi-local Reynolds number give a similar turbulent structure, and thus the resultant mean velocity and stress balance show collapsed profiles. On the other hand, typically, these physical quantities cannot be collapsed in the ideal gas cases, because of the changes in the semi-local Reynolds number. The results indicate the importance of the semi-local Reynolds number Re_τ^* rather than the density or temperature themselves and Re_τ^* is considered to be a similarity parameter for flows involving thermophysical variations.

For the velocity transformation which was proposed recently by Trettel and Larsson [22] and Patel *et al.* [23], the cases with a constant semi-local Reynolds number perfectly collapse on top of each other, compared with the ideal gas cases. However, they have a log-law offset to the incompressible case, indicating that this is related to a Mach number effect. Also, regarding the differences in the turbulent structures which affect the mean velocity profiles, the relevance to the velocity gradients is shown in the conditional averaged field for the ejection events of coherent turbulent structures in the near-wall region. As with Prandtl's mixing theory, there is a possibility that the turbulent properties induced by the changes of the semi-local Reynolds number can be identified and modeled by the velocity gradients.

Additionally, the verification of the spatially well developed temperature field evaluated with the temperature-velocity relations (i.e., Walz's equation) indicates that the analytical temperature-velocity relation cannot represent the temperature-velocity profiles in the outer layer of boundary layers, especially for the heated and cooled cases, because of the inapplicability of the equilibrium boundary layer assumptions that are used in the derivation of the temperature-velocity equation.

ACKNOWLEDGMENTS

This work was supported in part by Japan Society for the Promotion of Science (JSPS) Grant-in-Aid for Scientific Research (B) KAKENHI 18H01620 and the JSPS Invitation Fellowships for Research in Japan (S19017). A part of this research used computational resources of the K computer and the ITO computer, provided by the RIKEN Advanced Institute for Computational Science and the Research Institute for Information Technology, Kyushu University, respectively (Projects ID hp180158, hp190121, and hp200012).

APPENDIX A: ANALYSIS OF NONEQUILIBRIUM TERMS OF THE INTEGRATED TOTAL ENERGY EQUATION

The budgets of the nonequilibrium terms in Eq. (28) are shown in Fig. 14, which are classified as

$$\text{convective terms (streamwise)} = - \int_0^y \frac{\partial}{\partial x} \left\{ \frac{1}{2} \overline{\rho \tilde{u}_i \tilde{u}_i \tilde{u}} + \frac{1}{2} \overline{\rho u_i' u_i'' \tilde{u}} + \overline{\rho \tilde{u} \tilde{h}} \right\} dy, \quad (\text{A1})$$

$$\text{convective terms (wall normal)} = - \frac{1}{2} \overline{\rho \tilde{u}_i \tilde{u}_i \tilde{v}} - \frac{1}{2} \overline{\rho u_i' u_i'' \tilde{v}} - \overline{\rho \tilde{v} \tilde{h}}, \quad (\text{A2})$$

$$\text{turbulent diffusion terms (streamwise)} = - \int_0^y \frac{\partial}{\partial x} \left\{ \overline{\rho \tilde{u}_i u_i' u''} + \frac{1}{2} \overline{\rho u_i' u_i'' u''} + \overline{\rho u' h''} \right\} dy, \quad (\text{A3})$$

$$\text{turbulent diffusion terms (wall normal)} = - \overline{\rho \tilde{v} \tilde{v}''} - \frac{1}{2} \overline{\rho u_i' u_i'' v''}, \quad (\text{A4})$$

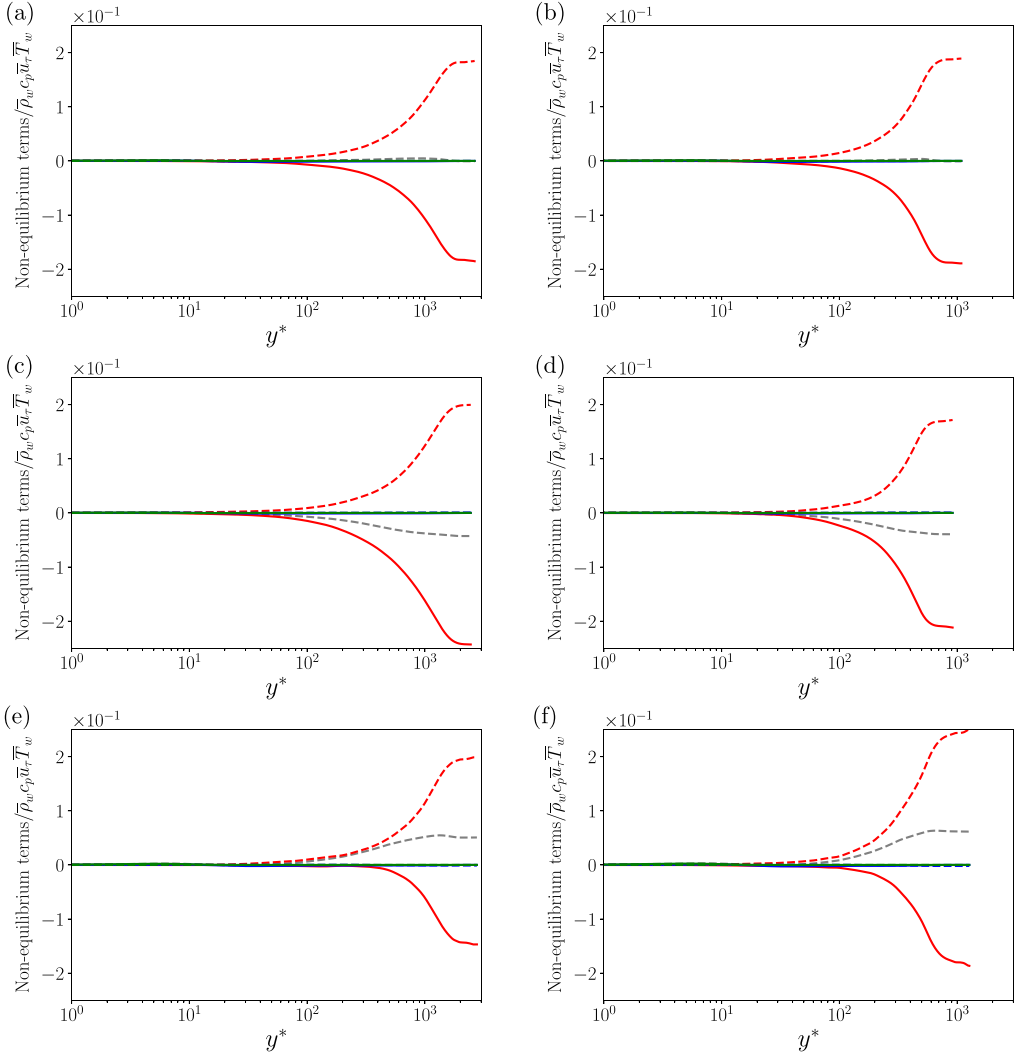


FIG. 14. Distributions of the nonequilibrium term components in the integrated total energy equation, shown in Eqs. (A1) to (A6). (a) AD, (b) ADcRe, (c) HE, (d) HEcRe, (e) CO, and (f) COcRe. Red lines, convective terms Eqs. (A1) and (A2); blue lines, turbulent diffusion terms Eqs. (A3) and (A4); green lines, viscous diffusion terms Eqs. (A5) and (A6); gray dashed lines, total nonequilibrium terms Eq. (28). Solid lines, wall-normal components; dashed lines, streamwise components. Blue and green lines are almost zero.

$$\text{viscous diffusion and local heat flux terms (streamwise)} = - \int_0^y \frac{\partial}{\partial x} \{ \bar{q}_x - \tilde{u}_i \bar{\tau}_{ix} - \overline{u_i'' \tau_{ix}} - \overline{u_i'' \tau_{ix}'} \} dy, \quad (\text{A5})$$

$$\text{viscous diffusion terms (wall normal)} = \tilde{v} \bar{\tau}_{yy} + \overline{u_i'' \tau_{iy}} + \overline{u_i'' \tau_{iy}'}. \quad (\text{A6})$$

In Fig. 14, the turbulent diffusion (blue lines) and viscous diffusion (and heat flux) terms (green lines) are negligible, and the convection terms (red lines) are dominant at the outer-layer regions for all of the cases, although the balances of the streamwise and wall-normal convective terms

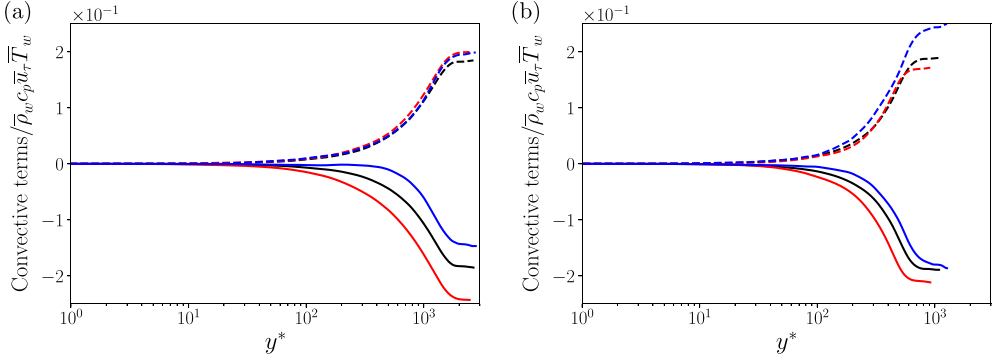


FIG. 15. Distributions of the convective terms Eqs. (A1) and (A2). (a) Ideal gas cases; (b) constant Re_τ^* cases. Solid lines, wall-normal components; dashed lines, streamwise components. Black, quasiadiabatic; red, heated; blue, cooled.

are different between the wall temperature cases. The two profiles almost balance each other in the adiabatic cases; on the other hand, the streamwise/wall-normal components become more dominant in the heated/cooled cases. As a result, the total nonequilibrium terms (gray dashed lines) do not become zero at outer-layer regions of wall heated and cooled cases. Furthermore, Fig. 15 shows a comparison of the convective terms, where it can be seen that for the ideal gas cases (a) the wall-normal components deviate from each other above $y^* \gtrsim 100$, while the streamwise components nearly collapse. It is indicated that the differences in the wall-normal convective components mainly affect the changes of the outer-layer nonequilibrium terms in the ideal gas cases. On the other hand, in Fig. 15(b) of the constant Re_τ^* cases, both streamwise and wall-normal components change between the different wall temperature cases: increase/decrease of the wall-normal components and decrease/increase of the streamwise ones in the heated/cooled case. Figure 16 shows the distributions of the wall-normal velocity, which is one of the variables contained in the wall-normal convective components. In the ideal gas cases, the heated case shows the largest and the cooled case the smallest values, which are consistent with the tendencies of the wall-normal convective components shown in Fig. 15(a). This suggests that for the ideal gas cases the differences in wall-normal convective components (i.e., differences in the total nonequilibrium terms in outer-layer regions) are caused by an increase or decrease of the wall-normal velocity. Similarly, also the constant Re_τ^*

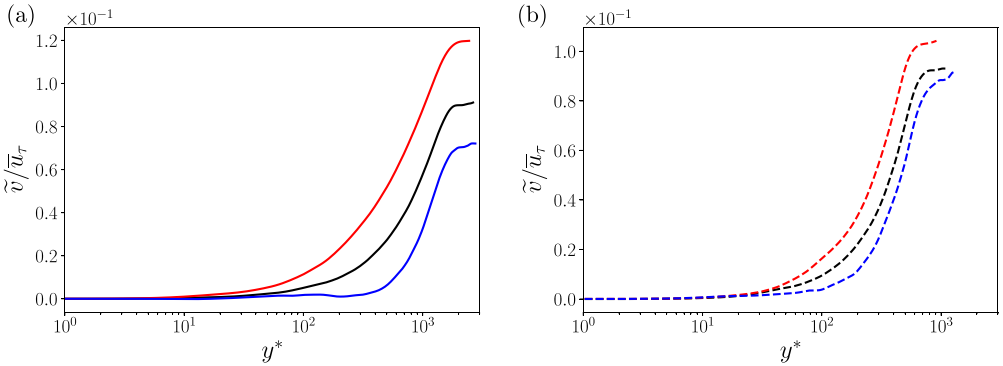


FIG. 16. Distributions of the mean wall-normal velocity normalized by the friction velocity. (a) Ideal gas cases; (b) constant Re_τ^* cases. Lines as in Table I.

cases show deviations of the wall-normal velocity distributions. However, the differences cannot be concluded as the dominant cause of the changes in the total nonequilibrium terms, because the streamwise convective components also contribute to the changes.

APPENDIX B: EFFECTS OF CONSTANT SEMI-LOCAL REYNOLDS NUMBER ON MEAN-VELOCITY SCALING

As shown in Fig. 6(f), for the constant semi-local Reynolds number cases, the van Driest transformed velocity profiles collapse well at the different wall temperature conditions. In this section, we investigate the reason behind the collapsed mean velocity and discuss how the constant semi-local Reynolds number affects the transformed mean-velocity profiles.

The van Driest transformation defined in Eq. (30) can be derived from the equilibrium inner-layer stress balance

$$\bar{\tau}_{xy} - \bar{\rho} \widetilde{u''v''} = \bar{\tau}_w. \quad (\text{B1})$$

In log-layer regions, the viscous stress $\bar{\tau}_{xy}$ is negligible and the Reynolds stress $\bar{\rho} \widetilde{u''v''}$ may be modeled by Prandtl's mixing length theory. The stress balance in Eq. (B1) now can be rewritten as

$$-\bar{\rho} \widetilde{u''v''} \approx \mu_t \frac{d\bar{u}}{dy} = \bar{\rho} \left(\kappa y \frac{d\bar{u}}{dy} \right)^2 = \bar{\tau}_w, \quad (\text{B2})$$

where $\kappa(=4.1)$ is the Kármán constant and $\mu_t = \bar{\rho}(\kappa y)^2(d\bar{u}/dy)$ is the turbulent eddy viscosity defined in Prandtl's mixing length theory. Equation (B2) may be written by the wall scaled quantities $\bar{u}^+ = \bar{u}/\bar{u}_\tau = \bar{u}/\sqrt{\bar{\tau}_w/\bar{\rho}_w}$ and $y^+ = y/L_\tau = \sqrt{\bar{\rho}_w}\sqrt{\bar{\tau}_w}y/\bar{\mu}_w$ as

$$\bar{\rho} \left(\kappa y \frac{d\bar{u}}{dy} \right)^2 = \bar{\rho} \left(\kappa y^+ \frac{d\bar{u}^+}{dy^+} \bar{u}_\tau \right)^2 = \bar{\tau}_w \frac{\bar{\rho}}{\bar{\rho}_w} \left(\kappa y^+ \frac{d\bar{u}^+}{dy^+} \right)^2 = \bar{\tau}_w. \quad (\text{B3})$$

Therefore,

$$\sqrt{\frac{\bar{\rho}}{\bar{\rho}_w}} \frac{d\bar{u}^+}{dy^+} = \frac{1}{\kappa y^+}. \quad (\text{B4})$$

Finally, integrating Eq. (B4) gives the logarithmic law of the wall with the definition of the van Driest transformed velocity \bar{u}_{vD}^+ as

$$\bar{u}_{vD}^+ \equiv \int_0^{\bar{u}^+} \sqrt{\frac{\bar{\rho}}{\bar{\rho}_w}} d\bar{u}^+ = \frac{1}{\kappa} \ln y^+ + B, \quad (\text{B5})$$

where B is a constant. Equation (B5) suggests that the van Driest transformed velocity \bar{u}_{vD}^+ follows the law of the wall in the log-layer regions.

On the other hand, another velocity transformation may be derived for the viscous sublayer. In the near-wall viscous dominated region, the Reynolds stress $\bar{\rho} \widetilde{u''v''}$ is negligible, so that the stress balance in Eq. (B1) may be written as

$$\bar{\tau}_{xy} \approx \bar{\mu} \frac{d\bar{u}}{dy} = \bar{\tau}_w. \quad (\text{B6})$$

Similar to the formulation in Eq. (B3), the stress balance in Eq. (B6) can be written by using the wall scaled quantities \bar{u}^+ and y^+ as

$$\bar{\mu} \frac{d\bar{u}}{dy} = \bar{\mu} \frac{d\bar{u}^+}{dy^+} \frac{\bar{u}_\tau}{L_\tau} = \bar{\tau}_w \frac{\bar{\mu}}{\bar{\mu}_w} \frac{d\bar{u}^+}{dy^+} = \bar{\tau}_w. \quad (\text{B7})$$

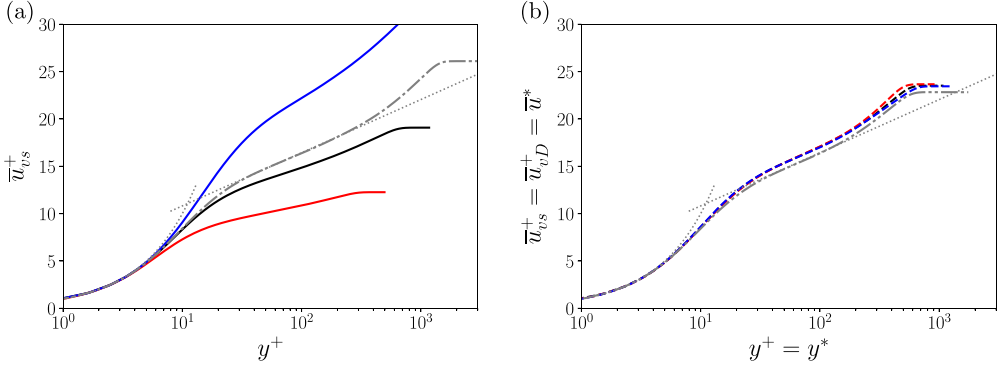


FIG. 17. Distributions of the transformed streamwise mean-velocity \bar{u}_{vs}^+ . (a) Ideal gas cases; (b) constant Re_τ^* cases. Gray dotted lines, incompressible law of the wall [$y^+ = u^+$ and $y^+ = \ln(u^+)/0.41 + 5.2$]; other lines, as in Table I.

Therefore, the linear law of the wall in the viscous sublayer is derived for the transformed velocity \bar{u}_{vs}^+ as

$$\bar{u}_{vs}^+ \equiv \int_0^{\bar{u}^+} \frac{\bar{\mu}}{\bar{\mu}_w} d\bar{u}^+ = y^+. \quad (\text{B8})$$

We note that the transformed velocity \bar{u}_{vs}^+ has been derived by Carvin *et al.* [54]. Equation (B8) suggests that the transformed velocity \bar{u}_{vs}^+ follows the law of the wall in the viscous sublayer.

In the constant Re_τ^* cases, the condition between the dynamic viscosity and density in Eq. (12) is imposed for ensuring the constant distributions of the semi-local Reynolds number. By imposing Eq. (12), Eqs. (B5) and (B8) yield

$$\bar{u}_{vD}^+ = \bar{u}_{vs}^+ \left(\because \sqrt{\frac{\bar{\rho}}{\bar{\rho}_w}} = \frac{\bar{\mu}}{\bar{\mu}_w} \right), \quad (\text{B9})$$

which means that the transformed velocity \bar{u}_{vD}^+ and also \bar{u}_{vs}^+ satisfy the law of the wall throughout the viscous sublayer and logarithmic region. Figure 17 shows the distributions of the transformed velocity \bar{u}_{vs}^+ . In the ideal gas cases of Fig. 17(a), the profiles agree well to the law of the wall in the viscous sublayer, although there are large discrepancies in the log region. On the other hand, all the compressible cases collapse each other from the wall to the log layer in the constant Re_τ^* cases as shown in Fig. 17(b). The collapsed profiles throughout the viscous sublayer and log layer in Fig. 17(b) indicate the validity of the analysis given in Eq. (B9), where \bar{u}_{vs}^+ becomes equivalent to \bar{u}_{vD}^+ when Eq. (12) is imposed. However, in the constant Re_τ^* cases, a log-law offset is observed for the compressible flows (also reported in Sec. IV B). The offset is equivalent to the differences in a constant of integration B , which is not guaranteed to be the same value of the incompressible case (≈ 5.2), even though Eq. (B9) is held.

As the above discussions, Eq. (B9) explains why the van Driest transformed velocity collapses each other from the wall to the log layer in the constant Re_τ^* cases. However, we stress that Eq. (B9) holds only when a constant distribution of the semi-local Reynolds number is imposed. On the other hand, the prior study [32] shows that the mean velocity and turbulent statistics agree well between the cases with similar semi-local Reynolds number distributions, including similar wall-normal variations. The prior study indicates that the distribution of the semi-local Reynolds number is a crucial parameter for the scaling of turbulent statistics and structures, and the density and viscosity themselves, as in Eq. (12), are not crucial parameters.

- [1] F. Aulery, A. Toutant, F. Bataille, and Y. Zhou, Energy transfer process of anisothermal wall-bounded flows, *Phys. Lett. A* **379**, 1520 (2015).
- [2] D. Dupuy, A. Toutant, and F. Bataille, Turbulence kinetic energy exchanges in flows with highly variable fluid properties, *J. Fluid Mech.* **834**, 05 (2018).
- [3] O. Reynolds, On the extent and action of the heating surface of steam boilers, *Int. J. Heat Mass Transfer* **3**, 163 (1961).
- [4] L. Crocco, Sulla trasmissione del calore da una lamina piana a un fluido scorrente ad alta velocità, *L'Aerotecnica* **12**, 181 (1932).
- [5] A. Walz, *Boundary Layers of Flow and Temperature* (MIT Press, Cambridge, MA, 1969).
- [6] L. Duan, I. Beekman, and M. P. Martin, Direct numerical simulation of hypersonic turbulent boundary layers. Part 3. Effect of Mach number, *J. Fluid Mech.* **672**, 245 (2011).
- [7] M. S. Shadloo, A. Hadjadj, and F. Hussain, Statistical behavior of supersonic turbulent boundary layers with heat transfer at $M_\infty = 2$, *Int. J. Heat Fluid Flow* **53**, 113 (2015).
- [8] A. Hadjadj, O. Ben-Nasr, M. S. Shadloo, and A. Chaudhuri, Effect of wall temperature in supersonic turbulent boundary layers: A numerical study, *Int. J. Heat Mass Transfer* **81**, 426 (2015).
- [9] M. V. Morkovin, Effects of compressibility on turbulent flows, *Mécanique de la Turbulence* (CNRS, Paris, 1962), pp. 367–380.
- [10] T. Cebeci and A. M. O. Smith, *Analysis of Turbulent Boundary Layers* (Academic Press, New York, 1974).
- [11] J. Gaviglio, Reynolds analogies and experimental study of heat transfer in the supersonic boundary layer, *Int. J. Heat Mass Transfer* **30**, 911 (1987).
- [12] M. W. Rubesin, Extra compressibility terms for Favre-averaged two-equation models of inhomogeneous turbulent flows, NASA Contractor Report NASA-CR-177556 (1990).
- [13] P. G. Huang, G. N. Coleman, and P. Bradshaw, Compressible turbulent channel flows: DNS results and modelling, *J. Fluid Mech.* **305**, 185 (1995).
- [14] S. E. Guarini, R. D. Moser, K. Shariff, and A. Wray, Direct numerical simulation of a supersonic turbulent boundary layer at Mach 2.5, *J. Fluid Mech.* **414**, 1 (2000).
- [15] Y.-S. Zhang, W.-T. Bi, F. Hussain, and Z.-S. She, A generalized Reynolds analogy for compressible wall-bounded turbulent flows, *J. Fluid Mech.* **739**, 392 (2014).
- [16] L. Duan, I. Beekman, and M. P. Martin, Direct numerical simulation of hypersonic turbulent boundary layers. Part 2. Effect of wall temperature, *J. Fluid Mech.* **655**, 419 (2010).
- [17] C. Zhang, L. Duan, and M. M. Choudhari, Direct numerical simulation database for supersonic and hypersonic turbulent boundary layers, *AIAA J.* **56**, 4297 (2018).
- [18] X. Chen, X. Li, and Z. Zhu, Effects of dimensional wall temperature on velocity-temperature correlations in supersonic turbulent channel flow of thermally perfect gas, *Sci. Chin.-Phys. Mech. Astron.* **62**, 064711 (2019).
- [19] C. Zhang, L. Duan, and M. M. Choudhari, Effect of wall cooling on boundary-layer-induced pressure fluctuations at mach 6, *J. Fluid Mech.* **822**, 5 (2017).
- [20] C. Brun, M. P. Boiarciuc, M. Haberkorn, and P. Comte, Large eddy simulation of compressible channel flow, *Theor. Comput. Fluid Dyn.* **22**, 189 (2008).
- [21] Y.-S. Zhang, W.-T. Bi, F. Hussain, X.-L. Li, and Z.-S. She, Mach-Number-Invariant Mean-Velocity Profile of Compressible Turbulent Boundary Layers, *Phys. Rev. Lett.* **109**, 054502 (2012).
- [22] A. Trettel and J. Larsson, Mean velocity scaling for compressible wall turbulence with heat transfer, *Phys. Fluids* **28**, 026102 (2016).
- [23] A. Patel, B. J. Boersma, and R. Pecnik, The influence of near-wall density and viscosity gradients on turbulence in channel flows, *J. Fluid Mech.* **809**, 793 (2016).
- [24] E. R. Van Driest, Turbulent boundary layer in compressible fluids, *J. Aeronaut. Sci.* **18**, 145 (1951).
- [25] G. N. Coleman, J. Kim, and R. D. Moser, A numerical study of turbulent supersonic isothermal-wall channel flow, *J. Fluid Mech.* **305**, 159 (1995).
- [26] A. Toutant and F. Bataille, Turbulence statistics in a fully developed channel flow submitted to a high temperature gradient, *Int. J. Therm. Sci.* **74**, 104 (2013).

- [27] S. Kawai, Heated transcritical and unheated non-transcritical turbulent boundary layers at supercritical pressures, *J. Fluid Mech.* **865**, 563 (2019).
- [28] R. K. Lobb, E. M. Winkler, and J. Persh, Experimental investigation of turbulent boundary layers in hypersonic flow, *J. Aeronaut. Sci.* **22**, 1 (1955).
- [29] Y. Morinishi, S. Tamano, and K. Nakabayashi, Direct numerical simulation of compressible turbulent channel flow between adiabatic and isothermal walls, *J. Fluid Mech.* **502**, 273 (2004).
- [30] J. Huang, G. L. Nicholson, L. Duan, M. M. Choudhari, and R. D. W. Bowersox, Simulation and modeling of cold-wall hypersonic turbulent boundary layers on flat plate, AIAA Paper No. 2020-0571 (2020).
- [31] P. S. Volpiani, M. Bernardini, and J. Larsson, Effects of a nonadiabatic wall on hypersonic shock/boundary-layer interactions, *Phys. Rev. Fluids* **5**, 014602 (2020).
- [32] A. Patel, J. W. R. Peeters, B. J. Boersma, and R. Pecnik, Semi-local scaling and turbulence modulation in variable property turbulent channel flows, *Phys. Fluids* **27**, 095101 (2015).
- [33] G. Urbin and D. Knight, Large-eddy simulation of a supersonic boundary layer using an unstructured grid, *AIAA J.* **39**, 1288 (2001).
- [34] M. Bernardini, I. Asproulias, J. Larsson, S. Pirozzoli, and F. Grasso, Heat transfer and wall temperature effects in shock wave turbulent boundary layer interactions, *Phys. Rev. Fluids* **1**, 084403 (2016).
- [35] S. K. Lele, Compact finite difference schemes with spectral-like resolution, *J. Comput. Phys.* **103**, 16 (1992).
- [36] D. Gaitonde and M. Visbal, Further development of a Navier-Stokes solution procedure based on higher-order formulas, AIAA Paper No. 99-0557 (1999).
- [37] S. Kawai and K. Fujii, Compact scheme with filtering for large-eddy simulation of transitional boundary layer, *AIAA J.* **46**, 690 (2008).
- [38] S. Kawai and S. K. Lele, Large-eddy simulation of jet mixing in supersonic crossflows, *AIAA J.* **48**, 2063 (2010).
- [39] S. Gottlieb and C.-W. Shu, Total variation diminishing Runge-Kutta schemes, *Math. Comput.* **67**, 73 (1998).
- [40] E. Lenormand, P. Sagaut, L. T. Phuoc, and P. Comte, Subgrid-scale models for large-eddy simulations of compressible wall bounded flows, *AIAA J.* **38**, 1340 (2000).
- [41] J. Jiménez, S. Hoyas, M. P. Simens, and Y. Mizuno, Turbulent boundary layers and channels at moderate Reynolds numbers, *J. Fluid Mech.* **657**, 335 (2010).
- [42] J. A. Sillero, J. Jiménez, and R. D. Moser, Two-point statistics for turbulent boundary layers and channels at Reynolds numbers up to $\delta^+ \approx 2000$, *Phys. Fluids* **26**, 105109 (2014).
- [43] F. Zonta, C. Marchioli, and A. Soldati, Modulation of turbulence in forced convection by temperature-dependent viscosity, *J. Fluid Mech.* **697**, 150 (2012).
- [44] J. F. Debiève, P. Dupont, D. R. Smith, and A. J. Smits, Supersonic turbulent boundary layer subjected to step changes in wall temperature, *AIAA J.* **35**, 51 (1997).
- [45] M. S. Shadloo and A. Hadjadj, Laminar-turbulent transition in supersonic boundary layers with surface heat transfer: A numerical study, *Numer. Heat Tr. A-Appl.* **72**, 40 (2017).
- [46] P. S. Volpiani, M. Bernardini, and J. Larsson, Effects of a nonadiabatic wall on supersonic shock/boundary-layer interactions, *Phys. Rev. Fluids* **3**, 083401 (2018).
- [47] S. J. Kline, W. C. Reynolds, F. A. Schraub, and P. W. Runstadler, The structure of turbulent boundary layers, *J. Fluid Mech.* **30**, 741 (1967).
- [48] J. M. Wallace, H. Eckelmann, and R. S. Brodkey, The wall region in turbulent shear flow, *J. Fluid Mech.* **54**, 39 (1972).
- [49] M. Marquillie, U. Ehrenstein, and J.-P. Laval, Instability of streaks in wall turbulence with adverse pressure gradient, *J. Fluid Mech.* **681**, 205 (2011).
- [50] J. Smagorinsky, General circulation experiments with the primitive equations, *Mon. Weather Rev.* **91**, 99 (1963).

- [51] K. Lam and S. Banerjee, On the condition of streak formation in a bounded turbulent flow, [Phys. Fluids](#) **4**, 306 (1992).
- [52] L. Brandt and H. C. de Lange, Streak interactions and breakdown in boundary layer flows, [Phys. Fluids](#) **20**, 024107 (2008).
- [53] P. Andersson, L. Brandt, A. Bottaro, and D. S. Henningson, On the breakdown of boundary layer streaks, [J. Fluid Mech.](#) **428**, 29 (2001).
- [54] C. Carvin, J. F. Debieve, and A. J. Smits, The near-wall temperature profile of turbulent boundary layers, AIAA Paper No. 88-0136 (1988).